International Journal of Nanomedicine

Dovepress
open access to scientific and medical research

Open Access Full Text Article

ORIGINAL RESEARCH

Fe_3O_4-Coated CNTs-Gum Arabic Nano-Hybrid Composites Exhibit Enhanced Anti-Leukemia Potency Against AML Cells via ROS-Mediated Signaling

Alyaa S Abdel Halim[1], Mohamed AM Ali[2,1], Fawad Inam[3,4], Abdulrahman M Alhalwan[5], Walid M Daoush[5,6]

[1]Department of Biochemistry, Faculty of Science, Ain Shams University, Cairo, 11566, Egypt; [2]Department of Biology, College of Science, Imam Mohammad Ibn Saud Islamic University (IMSIU), Riyadh, 11623, Kingdom of Saudi Arabia; [3]Department of Engineering and Computing, School of Architecture, Computing and Engineering, University of East London, London, UK; [4]Executive Principal Office, Oxford Business College, Oxford, OX1 2EP, UK; [5]Department of Chemistry, College of Science, Imam Mohammad Ibn Saud Islamic University, Riyadh, 11623, Kingdom of Saudi Arabia; [6]Department of Production Technology, Faculty of Technology and Education, Helwan University, Cairo, 11281, Egypt

Correspondence: Walid M Daoush, Email wmdaoush@imamu.edu.sa

Background: Prior studies on magnetite (Fe_3O_4) NPs and carbon nanotubes (CNTs) cytotoxic effects against acute myeloid leukemia (AML) are inconclusive rather than definitive.

Purpose: Investigation of the effects of Gum Arabic (GA)-stabilized/destabilized Fe_3O_4 NPs and CNTs, alone or in combination, on AML cell proliferation.

Methods: Hybrid NPs were synthesized, characterized, and assessed for their cytotoxicity against Kasumi-1, HL-60, and THP-1 in comparison to normal primary bone marrow $CD34^+$ cells. The molecular pathways of nanostructures' cytotoxicity were also investigated.

Results: The Fe_3O_4 NPs were effectively synthesized and attached to the surface of the CNTs, resulting in the formation of a novel hybrid through their interaction with the GA colloidal solution in an aqueous media. Although the evaluated nanostructured nanoparticles had significant growth suppression ability against the leukemia cell lines, with IC_{50} values ranging from 42.437 to 189.842 µg/mL, they exhibited comparatively modest toxicity towards normal hematopoietic cells (IC_{50}: 113.529–162.656 µg/mL). The incorporation of Fe_3O_4 NPs with CNTs in a hybrid nanocomposite significantly improved their effectiveness against leukemia cells, with the extent of improvement varying depending on the specific cell type. The nanostructured particles were stabilized by GA, which enhances their ability to inhibit cell proliferation in a manner that depends on the specific cell type. Also, nanoparticles exhibit cytotoxicity due to their capacity to stimulate the production of intracellular ROS, halt the cell cycle at the G1 phase, and induce apoptosis. This is supported by the activation of p53, BAX, cytochrome C, and caspase-3, which are triggered by ROS. The nanostructures lead to an increase in the expression of genes encoding proteins related to oxidative stress (SIRT1, FOXO3, NFE2L2, and MAP3K5) and cyclin-dependent kinase inhibitors (CDKN1A and CDKN1B) in response to ROS.

Conclusion: We provide an effective Fe_3O_4 NPs/CNTs nano-hybrid composite that induces apoptosis and has strong anti-leukemic capabilities. This hybrid nanocomposite is promising for in vivo testing and validation.

Keywords: acute myeloid leukemia, anti-leukemic properties, carbon nanotubes, iron oxide nanoparticles, oxidative stress, reactive oxygen species

Introduction

Acute myeloid leukemia (AML) is the most commonly diagnosed form of acute leukemia in older individuals. Enhanced comprehension of the biology and genetic structure of AML has resulted in improved evaluation of the risk associated with this disease. Although there have been some encouraging recent developments, the mainstay of treatment still

Received: 7 March 2024
Accepted: 3 July 2024
Published: 19 July 2024

Graphical Abstract

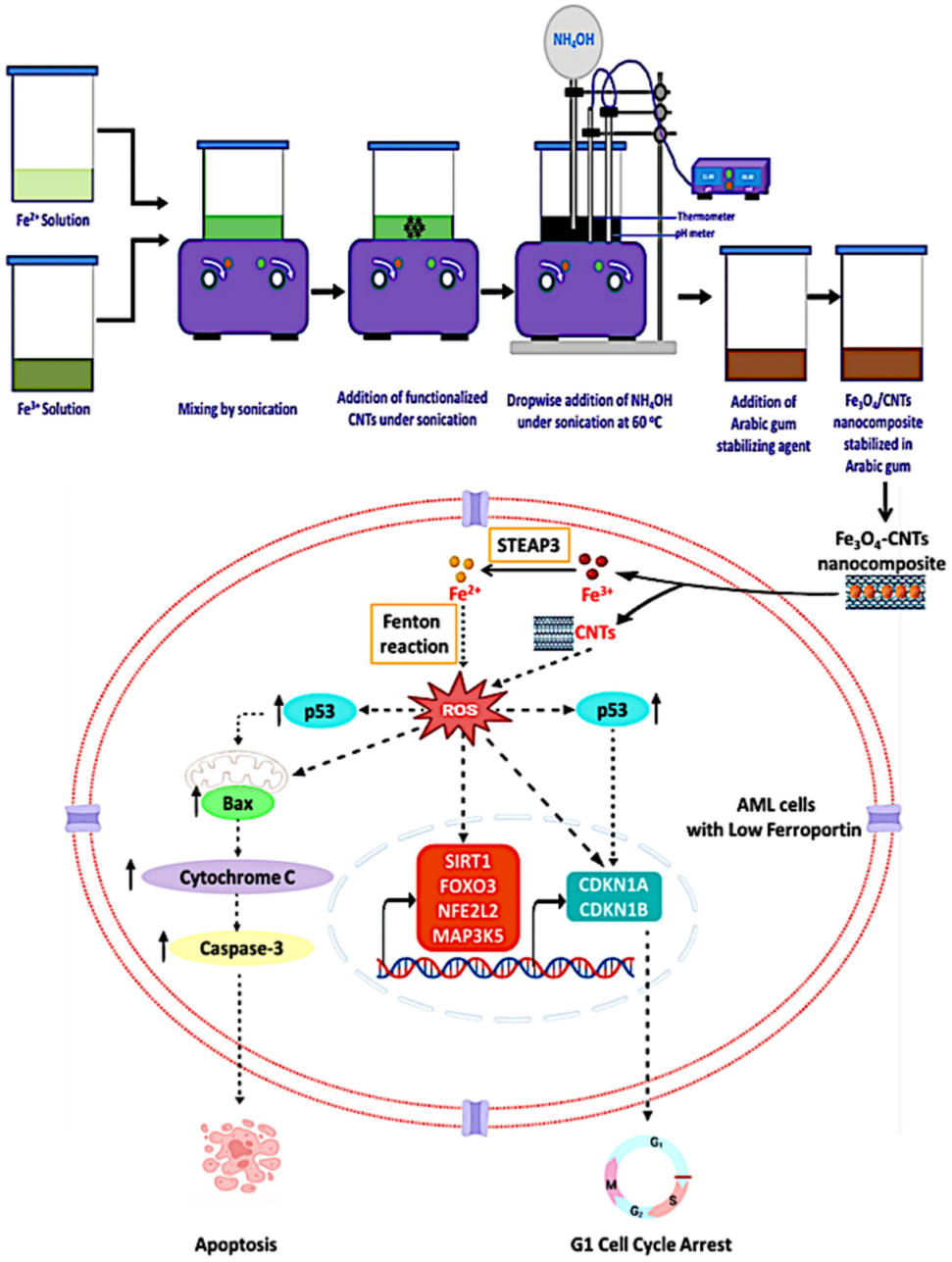

involves using a mix of cytarabine- and anthracycline-based treatment plans, along with allogeneic stem cell transplantation for suitable patients. Despite the implementation of many treatments, there has been no substantial improvement in the overall survival or disease-free survival rates of patients in clinical settings. Consequently, the prognosis for patients with AML is frequently characterized as extremely unfavorable or unsatisfactory.[1] The efficacy of various chemotherapeutic agents against AML has been hindered by several factors: (1) the narrow therapeutic window of these drugs, (2) the development of drug resistance in refractory AML, (3) inadequate impact on dormant cells like leukemic stem cells, and (4) unintended effects on non-target tissues. Therefore, there is still a need for the development of novel and targeted therapeutic approaches that can address the limitations of conventional chemotherapy.[2]

The emergence of nanoscale technology marks a significant development in the realm of cancer therapy. Due to their distinct physical and biological characteristics, nanotechnology-based medications have been included into cancer treatment and have significantly transformed the conventional methods of cancer therapy.[3] There has been a significant increase in research focused on designing and creating nanoparticle systems. These systems have resulted in the development of diverse material formulations that show promise therapeutic effects for treating different forms of cancer. Nanoparticles (NPs) are structures ranging in size from 1 to 100 nm, characterized by a significantly high surface-to-volume ratio. This unique feature gives rise to distinct behaviors not observed in larger particles of the same chemical makeup. The NPs are utilized in several biological applications due to their distinctive characteristics and their ability to penetrate cells and organelles owing to their nanoscale size.[4] Specifically, researchers have extensively studied inorganic NPs for their medicinal potential in treating malignant disorders. Inorganic NPs exhibit distinct physicochemical characteristics, including facile manufacturing, a high ratio of surface area to volume, stability, and the potential for surface modification to enhance their affinity and selectivity towards specific molecules.[5] Metallic nanoparticles such as Nobel metals like Au, Pt, Pd and Ag) are being used in different biomedical, applications due to their significant physicochemical properties. However, several investigations have listed their side effect on human. The cytotoxicity of silver NP (AgNPs) even at a low limit of exposure dosage (10–50 μg/mL) was reported in the literature,[6] whereas iron nanoparticles (FeNPs) at the level (100 μg/mL) showed low or no cytotoxicity as reported in previous report.[7] It was reported in the literature that; the iron based nanoparticles (FeNPs) are considered using in several sectors by FDA (US Food and Drug Administration), including magnetic resonance imaging for liver pathologies detection, iron deficiency anemia therapy in adults with chronic kidney disease.[8–11]

The biocompatible and biodegradable nature of iron oxide NPs, along with their easy manufacturing and capacity to be tailored and functionalized for specific purposes, make them highly promising for applications in medical cancer. Concurrently with the extensive range of their biological uses, there has been a rise in safety concerns regarding iron oxide NPs. Numerous investigations on the cytotoxicity of iron oxide NPs have been conducted. Iron oxide NPs are widely believed to have minimal or no harmful effects on cells. Nevertheless, studies have demonstrated that iron oxide NPs exhibit various harmful effects on cells, and diverse types of cells have displayed considerable vulnerability to the cytotoxicity of iron oxide NPs.[12]

Carbon nanotubes (CNTs) are a diverse group of nanomaterials that have a wide range of physical, chemical, mechanical, and biological properties. Due to their exceptional properties, CNTs have garnered significant interest in the field of biomedicine, namely in the realm of cancer treatment.[13] The extensive utilization of CNTs has prompted significant apprehensions regarding their safety. Despite several researches undertaken to assess the cytotoxicity of CNTs, the available data sometimes present conflicting results. Several studies have documented that CNTs can cause cytotoxicity in various cell lines, with the extent of toxicity being depending on both the duration and concentration of exposure. Nevertheless, alternative studies indicate the absence of cytotoxicity after administering CNTs.[14]

Carbon nanoparticles possess a significant surface area, which enables the potential for surface functionalization. Carbon nanomaterials are highly suitable for the attachment of NPs. Lately, there has been significant interest in the bonding of metal NPs to carbon nanomaterials. Metal NPs incorporated with carbon nanomaterials form nanohybrids that possess not only the distinct characteristics of the metal NPs and carbon nanomaterials, but also demonstrate improved features resulting from the interactions between these two components. The integration of metal NPs with carbon nanomaterials produces innovative and adaptable nanosystems that have significant potential in the field of biomedicine. Specifically, these nanosystems offer new possibilities for the development of cancer therapies based on nanotechnology.[15]

The uptake and behavior of nanosystems in biological environments are significantly influenced by three important parameters: particle size, coating, and stability. Typically, the iron oxide NPs rapidly clump together under conditions of normal body pH and in the presence of ions. Furthermore, the limited stability and varied size distribution in water are significant drawbacks of iron oxide NPs. To mitigate these drawbacks, the surface of iron oxide NPs can be coated with different polymers, particularly biopolymers like polysaccharides. This coating process results in the production of uniform, stable, and biocompatible iron oxide NPs.[16] The CNTs exhibit a propensity to congregate, resulting in their insolubility. In order to decrease the aggregation, the CNTs might be covered with synthetic or natural polymers.[17] Gum

Arabic (GA) is a naturally-occurring, non-toxic, water-loving, extensively-branched polysaccharide obtained from the exudates of Acacia senegal and Acacia seyal trees. Due to its biocompatibility and its ability to stabilize and emulsify, GA has been applied in the field of nanomedicine.[18]

Although many studies have been conducted to investigate the biological effects of magnetite (Fe_3O_4) NPs and CNTs, the cytotoxic effects of Fe_3O_4 NPs and CNTs remain contradictory. The current knowledge is inconclusive, with numerous contrasting outcomes. While several studies have indicated minimal or absent cytotoxicity, others have reported notable cytotoxic effects. Furthermore, the complete understanding of the possible lethal effects and the underlying molecular pathways of Fe_3O_4 NPs and CNTs on AML cells is still lacking. To reduce the ambiguity surrounding the toxicity of Fe_3O_4 NPs and CNTs, and to establish definitive evidence of their harmful effects on AML cells, we conducted a comprehensive assessment of the cytotoxic properties of GA-stabilized/destabilized Fe_3O_4 NPs and CNTs, both individually and in combination, on AML cell lines. Furthermore, the fundamental molecular pathways responsible for the cytotoxic effects of nanostructures were also examined.

Materials and Methods

Materials

Multi-walled CNTs (Lot No. mst-200) were purchased from Nanotech Co., Ltd. (South Korea). The CNTs had a length ranging from 10 to 50 μm, a diameter ranging from 15 to 30 nm, a Brunauer–Emmett–Teller (BET) surface area of around 200 m2/g, and a purity of 95%. The GA was obtained from exudates of Acacia senegal trees sourced from several regions of Saudi Arabia. All reagents utilized in nanostructures preparation and characterization, specifically ferric chloride hexahydrate, ferrous sulfate heptahydrate, ammonia solution, sulfuric acid, and nitric acid, are of laboratory grade.

Methods

Purification of GA and CNTs

A solution containing GA was created and purified to aid in stabilizing the CNTs, generated Fe_3O_4 NPs, and Fe_3O_4/CNTs nanocomposite. A stabilizing solution was made by boiling 1 gram of extracted GA powder in 100 milliliters of distilled water with continuous magnetic stirring until a gelatinous solution formed. The solution was filtered to eliminate any suspended contaminants, subsequently cooled, and stored at room temperature. As for CNTs, the unprocessed powder of the CNTs underwent a purification procedure that included subjecting it to heat treatments at a temperature of 450°C for a duration of 30 minutes. This process aimed to eliminate any organic binder that may potentially contaminate the surface of the powder. In addition, the specimen underwent multiple rinses using acetone to eliminate any extraneous organic contaminants. The CNTs powder generated after the heat treatment procedure underwent acid functionalization using ultrasonication at a frequency of 40 kHz and a temperature of 60°C in a combination of H_2SO_4 and HNO_3 for a duration of 15 minutes. This process was carried out to introduce functional groups onto the surface of the CNTs. The acquired CNTs were thoroughly rinsed with distilled water to eliminate any residual acids.

Synthesis and Stabilization of Fe_3O_4/CNTs Nano-Hybrid Composite

A calculated quantity of the purified CNTs was subjected to ultrasonication at a frequency of 40 kHz using the prepared solution of GA. This GA solution was employed to create a suspension of CNTs-GA hybrid. The Co-precipitation technique was used to prepare Fe_3O_4 NPs and Fe_3O_4/CNTs nanocomposites, which were stabilized with GA. Concisely, a solution containing 4 millimoles of ferric chloride hexahydrate and another solution containing 2 millimoles of ferrous sulphate heptahydrate were subjected to sonication at room temperature, with and without the calculated amounts of the CNTs to prepare Fe_3O_4/CNTs nanocomposite and Fe_3O_4 NPs, respectively. Ammonia solution (NH_4OH) is incrementally added to the previous solution until the co-precipitation process is finished. The pH of the solution is adjusted by using a pH glass electrode. Subsequently, the GA solution was introduced into the aforementioned combination while subjecting it to sonication for a duration of 15 minutes, resulting in the formation of the Fe_3O_4-GA and Fe_3O_4/CNTs-GA hybrid solution. Figure 1 depicts a schematic flowchart detailing the step-by-step co-precipitation synthesis process of the studied NPs. The volume fraction (Vf) of CNTs in the Fe_3O_4/CNTs nanocomposite particles was determined using

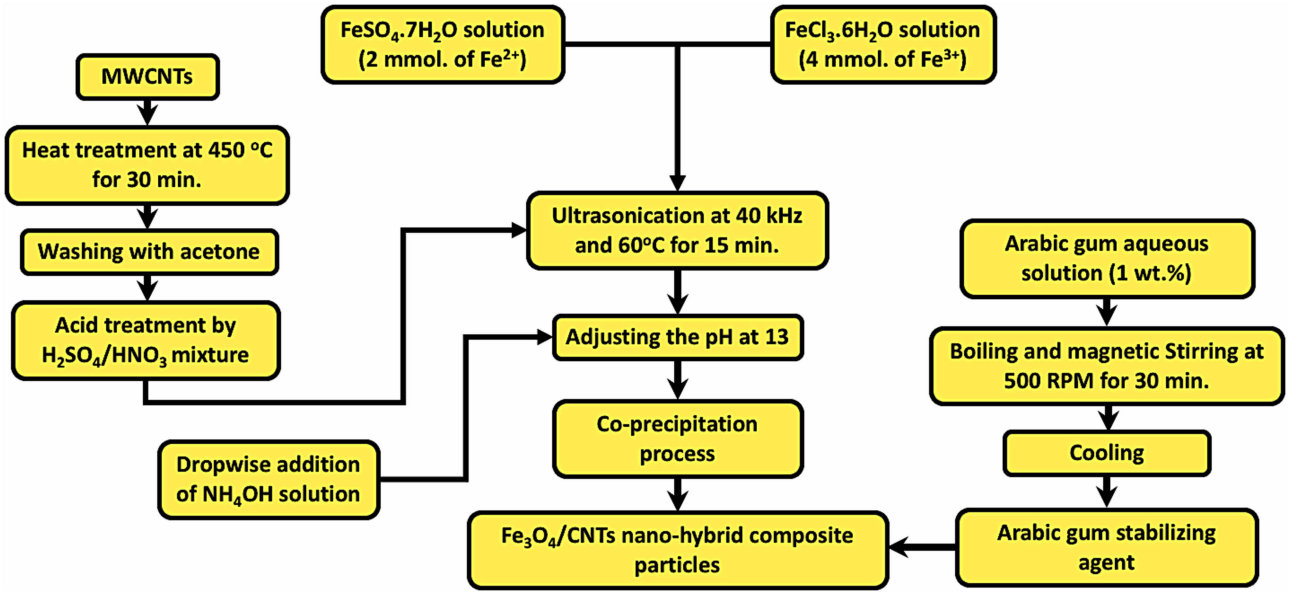

Figure 1 Experimental procedure design of GA-stabilized Fe_3O_4 and Fe_3O_4/CNTs nano-hybrid composite particles by co-precipitation process.

a simplified approximation based on the theoretical value of CNTs volume fraction, following the rule of mixtures. The analysis revealed that the calculated volume fraction for the synthesized 1 wt % Fe_3O_4/CNTs is around 5 Vol. % Fe_3O_4 /CNTs, with Fe_3O_4 having a density of 5.17 g/cm^3 and CNTs having a density of 1.74 g/cm^3.

Characterization and Investigations of NPs

The particle morphology, shape, and size of CNTs, as well as the produced Fe_3O_4 NPs and the Fe_3O_4/CNTs nanocomposites, were examined using a Field emission scanning electron microscope (FE-SEM) equipped with an energy-dispersive X-ray (EDS) unit (JEOL, JSM-7600F). A transmission electron microscope (TEM) of the model JEOL, JEM-1011 operated at an acceleration voltage of 300 kV was used to investigate the size, shape and surface morphology of the used CNTs. The X-ray diffractometer (XRD) (D8 DISCOVER, Bruker, MA, USA) was used to analyze the crystal structure and chemical content of the generated nanoparticles (NPs). The FTIR spectra of the produced NPs was measured using an FTIR-4600 Fourier Transform Infrared spectrometer manufactured by JASCO Corporation in Tokyo, Japan. The UV-visible spectra are also investigated by UV-T80 series of UV-Visible spectrophotometer (PG instruments Limited, Leicestershire, UK). The magnetization/field correlation was evaluated using a vibrating sample magnetometer (VSM) (7400 Series VSM, Lake Shore Cryotronics, Inc., OH, USA) to determine the magnetic characteristics and hysteresis loops. The magnetic characteristics that were measured consisted of saturation magnetization, retentivity, and coercivity. Due to the dependence of magnetization saturation and retentivity on the weight and volume of the sample, the acquired values were normalized by dividing them by the sample's weight. The magnetization was measured as a function of the applied field for all samples at room temperature. The magnetometer was calibrated using a standard nickel sphere. The analyses were conducted utilizing a maximum applied field of 2 Tesla.

Ferroportin Gene Expression Analysis

The quantitative polymerase chain reaction (qPCR) was used to determine the expression level of the gene encoding the iron-exporting protein Ferroportin (Solute carrier family 40 member 1, SLC40A1) in three leukemia cell lines: Kasumi-1 (representing acute myeloblastic leukemia), HL-60 (representing acute promyelocytic leukemia), and THP-1 (representing acute monocytic leukemia). The expression level was compared to that of normal hematopoietic cells (primary bone marrow $CD34^+$ cells). Concisely, the cells were collected by rinsing with phosphate buffered saline (PBS, Gibco, Thermo Fisher Scientific, Waltham, MA, USA), treated with 0.25% trypsin in PBS to detach them, and then spun at 300 x g for 5 minutes at 4°C. 1×10^7 cells were used to isolate total RNA using the RNeasy Plus Mini Kit (Cat. No. 74134, Qiagen, Hilden, Germany) following the instructions provided by the manufacturer. The reverse transcription process involved

converting approximately 1 µg of RNA into complementary DNA (cDNA) using the QuantiTect Reverse Transcription Kit (Cat. No. 205311, Qiagen, Hilden, Germany) according to the instructions provided by the manufacturer. The gene expression levels were quantitatively assessed using the QuantiTect SYBR Green PCR Kit (Cat. No. 204143, Qiagen, Hilden, Germany), in accordance with the manufacturer's recommendations. The QuantiTect Primer Assay (Cat. No. 249900, Qiagen, Hilden, Germany) was also used. The qPCRs were conducted using the Applied Biosystems QuantStudio 3 Real-Time PCR System, manufactured by Thermo Fisher Scientific in Waltham, MA, USA. The comparative Ct method ($2^{-\Delta\Delta Ct}$) was employed to examine relative gene expression, with ABL1 non-receptor tyrosine kinase serving as the endogenous reference gene. The gene expression levels were quantified in three replicates and shown as the ratio of gene expression in leukemia cells compared to the expression levels of the endogenous control, related to the normal primary bone marrow $CD34^+$ cells. The results are reported as the mean ± standard deviation.

In vitro Anti-Proliferative Activity

The GA-stabilized/destabilized Fe_3O_4 NPs and CNTs were tested for their cytotoxic effects on normal primary bone marrow $CD34^+$ cells (ATCC PCS-800-012) and three leukemia cell lines (Kasumi-1 [ATCC CRL-2724], HL-60 [ATCC CCL-240], and THP-1 [ATCC TIB-202]), which were obtained from the American Type Culture Collection (ATCC, Manassas, VA, USA). The cells were cultured according to the manufacturer's recommendations in either Iscove's Modified Dulbecco's Medium (IMDM) or RPMI 1640 Medium (Gibco, Thermo Fisher Scientific, Waltham, MA, USA). The culture medium was supplemented with 10% fetal bovine serum, 2 mM L-glutamine, 100 U/mL penicillin, 100 µg/mL streptomycin, and 25 µg/mL amphotericin B (Gibco, Thermo Fisher Scientific, Waltham, MA, USA). The cells were maintained at a temperature of 37°C and in an atmosphere containing 5% CO_2. Cell viability was assessed by employing the 3-[4,5-dimethylthiazol-2-yl]-2,5-diphenyltetrazolium bromide (MTT) Cell Proliferation Kit I (Cat. No. 11465007001, Roche, Basel, Switzerland) in accordance with the instructions provided by the manufacturer. In summary, cells were placed in 96-well flat-bottom microtiter plates with a density of 5×10^3 cells/well in 100 µL of culture media. They were then incubated for 24 hours at a temperature of 37°C and an environment containing 5% CO_2. After the incubation time, solutions containing GA-stabilized /destabilized Fe_3O_4 NPs and CNTs, either separately or together, were mixed with culture media to create concentrations of 7.8125, 15.625, 31.25, 62.5, 125, 250, 500, and 1000 µg/mL. These concentrations were then administered to the cells. In the negative control wells, an equal volume of growth media was supplied to the untreated cells. The cytotoxicity of doxorubicin, a standard anticancer medication sold by Sigma-Aldrich, Merck, Darmstadt, Germany, was assessed under identical conditions as a positive control. The cells were exposed to Fe_3O_4 NPs and CNTs that were either stabilized or destabilized by GA, either individually or in combinations, for a duration of 72 hours at a temperature of 37°C and an environment containing 5% CO_2. Following the incubation period, 10 µL of the MTT reagent (5 mg/mL in phosphate buffered saline) was introduced to each well, resulting in a final concentration of 0.5 mg/mL. The microtiter plates were then incubated for 4 hours at a temperature of 37°C in an environment containing 5% CO_2. Subsequently, 100 µL of the solubilization solution was added to each well. The microtiter plates were then left overnight in the incubator at a temperature of 37°C and an environment containing 5% CO_2. This was done to dissolve the purple formazan crystals. The samples were analyzed for absorbance at a wavelength of 570 nm using the xMark Microplate Absorbance Spectrophotometer (Bio-Rad Laboratories, Hercules, CA, USA). Three cell viability assays were conducted for each cell line, with each nanoformulation tested in triplicate at a specific concentration in each assay. Cell viability was determined using the formula: cell viability (percentage) = (absorbancetreated / absorbanceuntreated) × 100. The inhibitory concentration 50% (IC_{50}) of each nanoformulation was determined by measuring its in vitro growth inhibition effect. IC_{50} is defined as the concentration (µg/mL) at which the treated cells show a 50% growth inhibition compared to the untreated control cells. The IC_{50} values were calculated as the mean ± standard deviation (SD) of three independent measurements. The IC_{50} value was calculated using the GraphPad Prism 9.0 software (GraphPad, Dotmatics, Boston, MA, USA) by nonlinear regression curve fitting, specifically by plotting Log [concentration] against normalized response.

Determination of Intracellular Iron Content

The impact of GA-stabilized/destabilized Fe_3O_4 NPs and CNTs, either individually or in combinations, on the levels of iron inside the cells was evaluated by subjecting the cells to the predetermined IC_{50} concentration of each

nanoformulation for a duration of 48 hours at a temperature of 37°C and a CO_2 concentration of 5%. To the untreated cells, an equal volume of PBS was introduced. The quantification of total iron content was performed in the cell lysates using a colorimetric technique. In summary, cells were collected by centrifugation at 500 x g for a duration of 5 minutes at a temperature of 4°C. Subsequently, the cells were rinsed twice with chilled PBS. Afterwards, the liquid portion above was discarded and the solid mass of cells was gathered. The cells were broken down using a Cell Extraction Buffer (containing Tris, NaCl, EDTA, EGTA, NaF, $Na_4P_2O_7$, Na_3VO_4, Triton X-100, glycerol, SDS, and deoxycholate) provided by Invitrogen, Thermo Fisher Scientific. The buffer was supplemented with a Protease Inhibitor Cocktail from Sigma-Aldrich, Merck KGaA, and Phenylmethanesulfonyl fluoride (PMSF) from Sigma-Aldrich, Merck KGaA. The cells were kept on ice for 30 minutes at a concentration of 1×10^7 cells/mL, following the instructions provided by the manufacturer. The lysates were clarified using centrifugation at a speed of 13,000 rpm for a duration of 10 minutes at a temperature of 4°C. The Bio-Rad Protein Assay was used to assess the concentration of total protein in the cleared cell lysates, following the directions provided by the manufacturer. After the cell lysates were cleaned, they were divided into smaller portions and frozen at a temperature of −80°C for future study. The Iron Assay Kit (ab83366, Abcam, Cambridge, UK) was used to estimate the total iron levels, following the manufacturer's instructions. The intracellular iron contents were quantified in triplicate, adjusted for sample dilution, standardized to the total protein content of the cell lysates, and reported as nmol/mg total protein of cell lysate (mean ± SD, n=3).

Measurement of Intracellular ROS Levels

The levels of reactive oxygen species (ROS) within the cells were measured using the Fluorometric Intracellular ROS Kit (Cat. No. MAK143, Sigma-Aldrich, Merck, Darmstadt, Germany) as per the instructions provided by the manufacturer. The test relies on the idea that ROS interact with a fluorogenic sensor located in the cytoplasm, leading to the production of a fluorometric product that is directly proportional to the quantity of ROS present. In summary, the cells were placed in 96-well microplates with poly-D-lysine coating, black walls, and optically clear flat bottoms. The cells were seeded at a density of 50×10^3 cells per well, with each well containing 90 µL of culture media. The cells were then incubated for 24 hours at a temperature of 37°C and in an environment with 5% CO_2. Subsequently, 100 µL of the Master Reaction Mix was introduced into each well, and the cells were subjected to incubation for 1 hour at a temperature of 37°C in an environment containing 5% CO_2. Subsequently, the cells were exposed to the predetermined IC_{50} concentration of each nanoformulation, which was dissolved in 20 µL of PBS per well. Equivalent volume of PBS was added to the negative control wells, which contained untreated cells. The ability of doxorubicin (Adriamycin; Sigma-Aldrich, Merck, Darmstadt, Germany) to produce ROS was assessed using the same experimental settings as a positive control. Following a further 48-hour incubation at a temperature of 37°C and a CO_2 concentration of 5%, the fluorescence intensity was quantified using the FluoStar Omega multi-mode microplate reader (BMG Labtech, Ortenberg, Germany). The reader was set to an excitation wavelength of 490 nm and an emission wavelength of 525 nm ($\lambda ex= 490/\lambda em = 525$ nm). The experiment was conducted in triplicates for each nanoformulation in every cell line. ROS levels were quantified by calculating the fold change of relative fluorescence units (RFU) in treated cells compared to the negative control (untreated cells). The results were reported as the mean ± standard deviation (SD) of three separate measurements.

Mechanistic Investigations

In order to investigate the molecular mechanisms responsible for the cytotoxic effects of the prepared nanostructures on leukemia cell lines, we treated the most sensitive cell line (HL-60) with the predetermined IC_{50} of each nanoformulation. We then conducted various tests to determine the mechanisms involved, including estimating the number of apoptotic cells, analyzing the distribution of cell-cycle phases, measuring the levels of apoptosis-related proteins, and quantifying the expression levels of genes encoding oxidative stress-related proteins and cyclin-dependent kinase inhibitors.

Determination of Apoptotic Cells

In order to determine if the prepared nanostructures have a toxic effect on leukemia cell lines by causing apoptosis, the HL-60 cell line, which is the most responsive, was exposed to each nanoformulation for 48 hours at a temperature of 37°C and a CO_2 concentration of 5%. The percentage of cells undergoing apoptosis was measured using the BD FITC Annexin V Apoptosis Detection Kit I (Cat. No. 556547, BD Biosciences, San Jose, CA, USA) following the instructions

provided by the manufacturer. In summary, the cells were rinsed twice with chilled PBS and thereafter subjected to centrifugation at 300 x g for 5 minutes at ambient temperature. The liquid portion was removed and the clumped cells were mixed again in a solution called 1X Annexin V Binding Buffer, with a concentration of 1×10^6 cells per milliliter. 100 µL of the cell solution was transferred to a 5 mL tube, and then 5 µL of FITC Annexin V and 5 µL of propidium iodide (PI) were added. The cells were gently agitated and placed in a dark environment at room temperature for a duration of 15 minutes. Afterwards, 400 µL of 1X Annexin V Binding Buffer was introduced, and the cells were collected using a BD Accuri C6 Flow Cytometer and examined using BD Accuri C6 software (BD Biosciences, San Jose, CA, USA).

Estimation of Cell-Cycle Phase Distribution

In order to assess the impact of the prepared nanostructures on the distribution of cell-cycle phases, the HL-60 cell line, which exhibited the highest sensitivity, was exposed to each nanoformulation for a duration of 48 hours at a temperature of 37°C and a CO_2 concentration of 5%. The distribution of cell-cycle phases was then determined using the BD CycleTest Plus DNA Reagent Kit (Cat. No. 340242, BD Biosciences, San Jose, CA, USA) following the instructions provided by the manufacturer. Concisely, the cells were rinsed twice with Buffer Solution, and thereafter subjected to centrifugation at 300 x g for 5 minutes at room temperature. The liquid portion was discarded, and the solid portion containing cells was mixed with Buffer Solution to achieve a concentration of 1×10^6 cells per milliliter. The cell solution was thereafter subjected to centrifugation at 400 x g for a duration of 5 minutes at ambient temperature, following which the liquid portion above the sediment was discarded. The lipids of the cell membrane were dissolved using a nonionic detergent. The cell cytoskeleton and nuclear proteins were removed using trypsin. Cellular RNAs were broken down using RNase. The nuclear chromatin was stabilized using spermine. Finally, the DNA was stained with propidium iodide (PI) according to the instructions provided by the manufacturer. The cells were collected using a BD Accuri C6 Flow Cytometer and examined using BD Accuri C6 software (BD Biosciences, San Jose, CA, USA).

Determination of Apoptosis-Related Proteins Level

The impact of the produced nanostructures on apoptosis-related proteins was evaluated by subjecting the most susceptible cell line (HL-60) to each nanoformulation for 48 hours at a temperature of 37°C and a CO_2 concentration of 5%. The levels of apoptosis-associated proteins, such as p53, Bax, Bcl-2, Cytochrome C, and Caspase-3, were measured in the cell lysates using Enzyme-Linked Immunosorbent Assays (ELISAs). In summary, cells were collected by centrifugation at 500 x g for a duration of 5 minutes at a temperature of 4°C. The cells were subsequently rinsed twice with chilled PBS. Afterwards, the liquid portion above the sediment was discarded and the solid mass of cells was gathered. The cells were lysed in a Cell Extraction Buffer containing various components including Tris, NaCl, EDTA, EGTA, NaF, $Na_4P_2O_7$, Na_3VO_4, Triton X-100, glycerol, SDS, and deoxycholate. The lysing process was carried out on ice for 30 minutes at a concentration of 1×10^7 cells per milliliter of Cell Extraction Buffer. A Protease Inhibitor Cocktail and Phenylmethanesulfonyl fluoride (PMSF) were added to the buffer as instructed by the manufacturer. The Cell Extraction Buffer was obtained from Invitrogen, Thermo Fisher Scientific, and the Protease Inhibitor Cocktail and PMSF were obtained from Sigma-Aldrich, Merck KGaA. The lysates were clarified using centrifugation at a speed of 13,000 rpm for a duration of 10 minutes at a temperature of 4°C. The Bio-Rad Protein Assay was used to assess the concentration of total protein in the cleared cell lysates, following the directions provided by the manufacturer. The cell lysates were cleaned, divided into smaller portions, and frozen at a temperature of −80°C for future ELISAs. We used commercially available ELISA kits to measure the concentrations of apoptosis-related proteins. These kits included the Human p53 ELISA Kit (ab171571, Abcam, Cambridge, UK), Human Bax ELISA Kit (ab199080, Abcam, Cambridge, UK), Human Bcl-2 ELISA Kit (ab272102, Abcam, Cambridge, UK), Human Cytochrome C ELISA Kit (Cat. No. BMS263, Invitrogen, Thermo Fisher Scientific, Waltham, MA, USA), and Human cleaved (active) Caspase-3 ELISA Kit (Cat. No. KHO1091, Invitrogen, Thermo Fisher Scientific, Waltham, MA, USA). We followed the protocols provided by the manufacturers. The levels of apoptosis-related proteins were quantified in three replicates, adjusted for sample dilution, standardized to the overall protein content of the cell lysates, and reported as ng/mg total protein of cell lysate (mean ± SD, n=3).

Gene Expression Quantitation

The impact of the prepared nanostructures on the expression of genes that encode proteins related to oxidative stress (SIRT1, FOXO3, NFE2L2, and MAP3K5) and genes that encode inhibitors of cyclin-dependent kinases (p21 [CDKN1A] and p27 [CDKN1B]) was investigated. This was done by subjecting the most susceptible cell line (HL-60) to each nanoformulation for 48 hours at a temperature of 37°C and a CO_2 concentration of 5%. Quantitative polymerase chain reaction (qPCR) was used to evaluate the gene expression levels of SIRT1, FOXO3, NFE2L2, MAP3K5, CDKN1A, and CDKN1B. Concisely, the cells were collected by rinsing with PBS, treated with 0.25% trypsin in PBS to detach them, and then subjected to centrifugation at 300 x g for 5 minutes at 4°C. 1×10^7 cells were used to extract total RNA using the RNeasy Plus Mini Kit (Cat. No. 74134, Qiagen, Hilden, Germany) following the instructions provided by the manufacturer. The reverse transcription process involved converting approximately 1 µg of RNA into complementary DNA (cDNA) using the QuantiTect Reverse Transcription Kit (Cat. No. 205311, Qiagen, Hilden, Germany) according to the instructions provided by the manufacturer. The gene expression levels were quantitatively assessed using the QuantiTect SYBR Green PCR Kit (Cat. No. 204143, Qiagen, Hilden, Germany), in accordance with the manufacturer's recommendations. QuantiTect Primer Assays (Cat. No. 249900, Qiagen, Hilden, Germany) were also used. The qPCRs were conducted using the Applied Biosystems QuantStudio 3 Real-Time PCR System, manufactured by Thermo Fisher Scientific in Waltham, MA, USA. The analysis of relative gene expression was conducted using the comparative Ct method ($2^{-\Delta\Delta Ct}$), with ABL1 non-receptor tyrosine kinase serving as the endogenous reference gene. The gene expression levels were quantified in three replicates and reported as the ratio of gene expression in leukemia cells compared to the expression levels of the endogenous control, relative to the untreated cells. The results are presented as the mean ± standard deviation.

Statistical Analysis

The normality of the data distribution was assessed using the Kolmogorov–Smirnov test. The results were presented as the mean ± standard deviation (SD) and were compared using one-way analysis of variance (ANOVA), followed by Tukey's multiple comparison test. The statistical analyses of the data were performed using the GraphPad Prism 9.0 program (GraphPad, Dotmatics, Boston, MA, USA).

Results

Herein, an effective and direct approach was described for the simple combination of high-content superparamagnetic Fe_3O_4 nanoparticles of definite size uniformly deposited on the surface of high-mechanically strength multi-walled CNTs as nanocontainer template which is dispersed and stabilized in aqueous solution of biocompatible Gum Arabic biopolymer. Our results suggest a novel and simple approach for controlling the loading and size distribution of Fe_3O_4 on the surface of multi-walled CNTs, which leads to further development of CNT-based nanomaterials. Noteworthy, although numerous studies have been conducted to examine the biological effects of magnetite (Fe_3O_4) NPs and CNTs, the cytotoxic effects of Fe_3O_4 NPs and CNTs remain inconsistent. The current state of knowledge is inconclusive, as there are a multitude of contrasting results. Although several studies have suggested that cytotoxicity is minimal or nonexistent, others have reported significant cytotoxic effects. Additionally, the potential deleterious effects and the underlying molecular pathways of Fe_3O_4 NPs and CNTs on AML cells are still not fully understood.

Surface Treatments of CNTs

The initial stage of the treatment procedure for the as received CNTs was subjecting them to a temperature of 450°C in an oven for a duration of 30 minutes. This was done to eliminate certain volatile organic substances, such as the binding agent, that are introduced into the particles during the manufacturing process. Following the heat treatment of the CNTs, they were subjected to a washing process using acetone to eliminate any soluble organic contaminants that may have been generated during the heat treatment. The CNTs underwent acid treatments using a combination of H_2SO_4 and HNO_3. The TEM image in Figure 2a displays the multi-walled CNTs under investigation, with an approximate hollow core of inner diameter of 4.5 nm and outer diameter of 19 nm with a multiwall graphitic structure. Figure 2b displays the X-ray diffraction (XRD) pattern of the examined CNTs. The diffraction peaks were observed at angles of 26°, 43°, 53°,

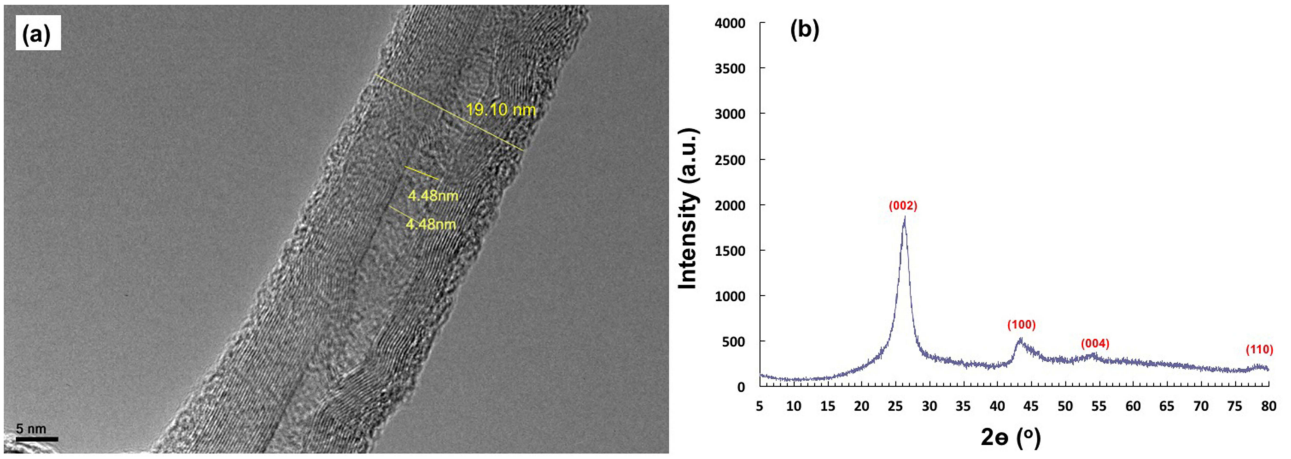

Figure 2 TEM (**a**) and XRD pattern (**b**) of the investigated CNTs.

and 79°, which correspond to the crystalline planes 002, 100, 004, and 110, respectively. These assignments are based on the joint committee on powder diffraction standards (JCPDS) # 96–101-1061.

Synthesis and Stabilization of Fe_3O_4 and Fe_3O_4/CNTs Nano-Hybrid Composite in GA

The process of depositing Fe_3O_4 NPs onto the surface of CNTs was investigated in the presence of ultrasonic radiation. The deposition solution consisted of essential components, namely ferrous sulphate heptahydrate and ferric chloride hexahydrate, which included salts of ferrous and ferric ions. Ammonium hydroxide was employed as a precipitating agent. For the precipitation process using ammonia solution, it is necessary to adjust the pH of the solution to approximately 12.5 and maintain a temperature of around 67°C. Figure 3 displays the produced Fe_3O_4 NPs, along with the Fe_3O_4/CNTs nanocomposite, which is evenly distributed in the GA aqueous solution. The results suggest that 1 wt. % GA aqueous solution is a suitable stabilizing agent for the synthesized NPs. The Fe_3O_4 and the Fe_3O_4/CNTs NPs were evenly distributed over an extended duration.

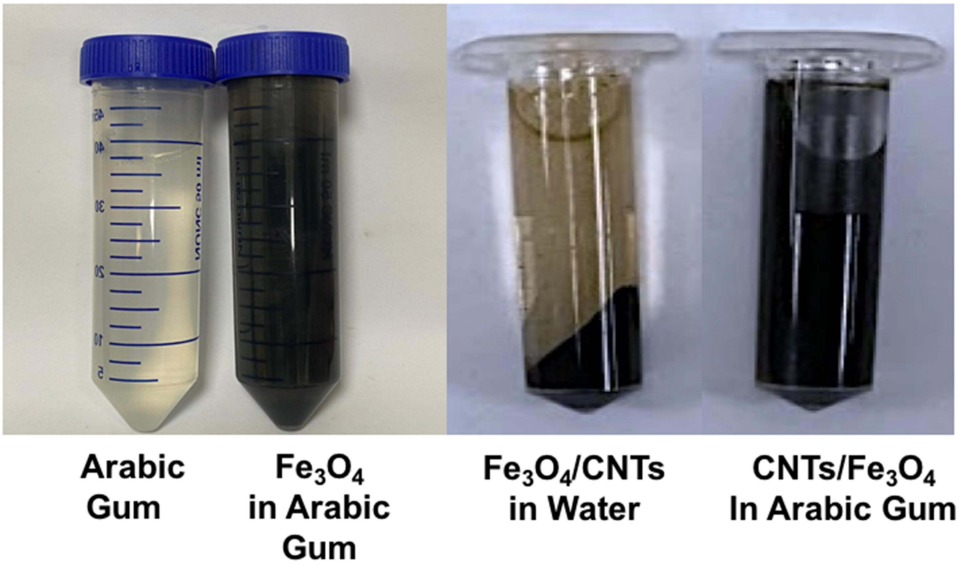

Figure 3 The produced Fe_3O_4 NPs and the Fe_3O_4/CNTs nano-hybrid composite dispersed and stabilized in GA solution.

FTIR and UV-Visible Spectrum of the Nano-Hybrid Composite

GA was employed as a stabilizing agent for the synthesized Fe_3O_4 and Fe_3O_4/CNTs nanocomposite particles, facilitating their dispersion in aqueous solutions and resulting in the formation of a stable colloidal solution. Figure 4a and b displays the FTIR spectrum illustrating the various functional groups found in the GA as well as after the combinations with the prepared nanoparticles (Fe_3O_4 and Fe_3O_4/CNTs). Also Figure 4c represent the absorption peaks of the UV-Visible spectra for the investigated nanoparticles stabilized with GA in aqueous solution. Figure 5 depicts a schematic illustration of the anticipated interaction between the carbohydrate and glycoprotein chains of the GA and the Fe_3O_4/CNTs nanocomposite particles.

Particle Shape, Size and Morphology of the NPs

SEM micrographs of the deposited Fe_3O_4 NPs at various magnifications and particles size distribution are presented in Figure 6a and b. The Fe_3O_4 NPs that were deposited have a nearly spherical morphology, with a particle size ranging from 28 to 49 nm. Furthermore, the nanoscale Fe_3O_4 NPs were formed and made stable in the aqueous solution containing the GA stabilizing agent. The optimal reaction temperature of around 67°C was determined by monitoring the course of the reaction and ensuring that all iron ions in the solution were transformed into Fe_3O_4 NPs. Figure 7 displays high-resolution scanning electron microscopy micrographs of the manufactured Fe_3O_4/CNTs nanocomposite particles, together with both low and high magnifications. Additionally, the figure includes EDS compositional analysis of the particles. The findings revealed that the acid functionalized CNTs were adorned with the Fe_3O_4 NPs. The EDS compositional analysis indicated that the produced Fe_3O_4/CNTs nanocomposite particles composed primarily of iron metal and elemental oxygen, with a composition of 1 wt.% Fe_3O_4/CNTs.

XRD and Phase Analysis of the NPs

Figure 8 displays the XRD patterns of both the Fe_3O_4 NPs and the Fe_3O_4/CNTs nanocomposites. The results indicate that the observed peaks are caused by the existence of specific diffraction peaks, namely 111, 220, 311, 222, 400, 422, 511, 440, 531, 620, 533, 622, and 444. These peaks correspond to the JCPDS 79–0419 of the Fe_3O_4 structure. No extra or foreign peaks were detected. The results suggest that the prepared Fe_3O_4 NPs have a high level of purity. Furthermore, Figure 8 depicts the XRD pattern of the Fe_3O_4/CNTs nanocomposites. The results indicate that the detected peaks are a result of the presence of Fe_3O_4 NPs that were deposited onto the surface of the CNTs.

Magnetic Properties of the Nano-Hybrid Composite

Figure 9a–c depicts the hysteresis loops of the examined CNTs, Fe_3O_4 NPs, and the nanocomposite particles of Fe_3O_4 /CNTs. The saturation magnetizations (Ms), retentivity (Mr), and coercivity (Hc) of the studied CNTs, Fe_3O_4 NPs, and Fe_3O_4/CNTs nanocomposite were determined at room temperature using a maximum applied field of 2T, as presented in Figure 9. The Ms value of Fe_3O_4/CNTs nanocomposite particles (52.172 emu/g; see Figure 9c) is lower than that of the Fe_3O_4 NPs (57.741 emu/g; see Figure 9b), possibly because of the influence of the 1 wt. % content of CNTs (Ms 2.0269 emu/g; see Figure 9a) in the Fe_3O_4/CNTs nanocomposite particles. Additionally, the Fe_3O_4 sample at the nanoscale exhibits superparamagnetism and a saturation magnetization (Ms) value that is lower than that of the bulk Fe_3O_4 sample (92 emu/g). In addition, Figure 9 illustrates the hysteresis vanished with a little retentivity value of 0.17078 emu/g and a coercivity (Hc) of 117.99 G, 1.40040 emu/g and coercivity (Hc) of 38.913 G, 0.80027 emu/g and coercivity (Hc) of 27.054 G in case of CNTs (see Figure 9a), Fe_3O_4 NPs (see Figure 9b) and Fe_3O_4/CNTs nanocomposite particles (see Figure 9c), respectively. This suggests that there is no long range of magnetic dipole-dipole interaction among the assemblies of the superparamagnetic NPs. Consequently, the Fe_3O_4 NPs and Fe_3O_4/CNTs nanocomposite particles exhibit magnetization easily when exposed to an applied magnetic field, with retentivity values of 1.40040 emu/g (see Figure 9b) and 0.80027 emu/g (see Figure 9c), respectively. A potential cause for this distinct structure is the independent thermal fluctuation of minuscule ferromagnetic domains within the particles.

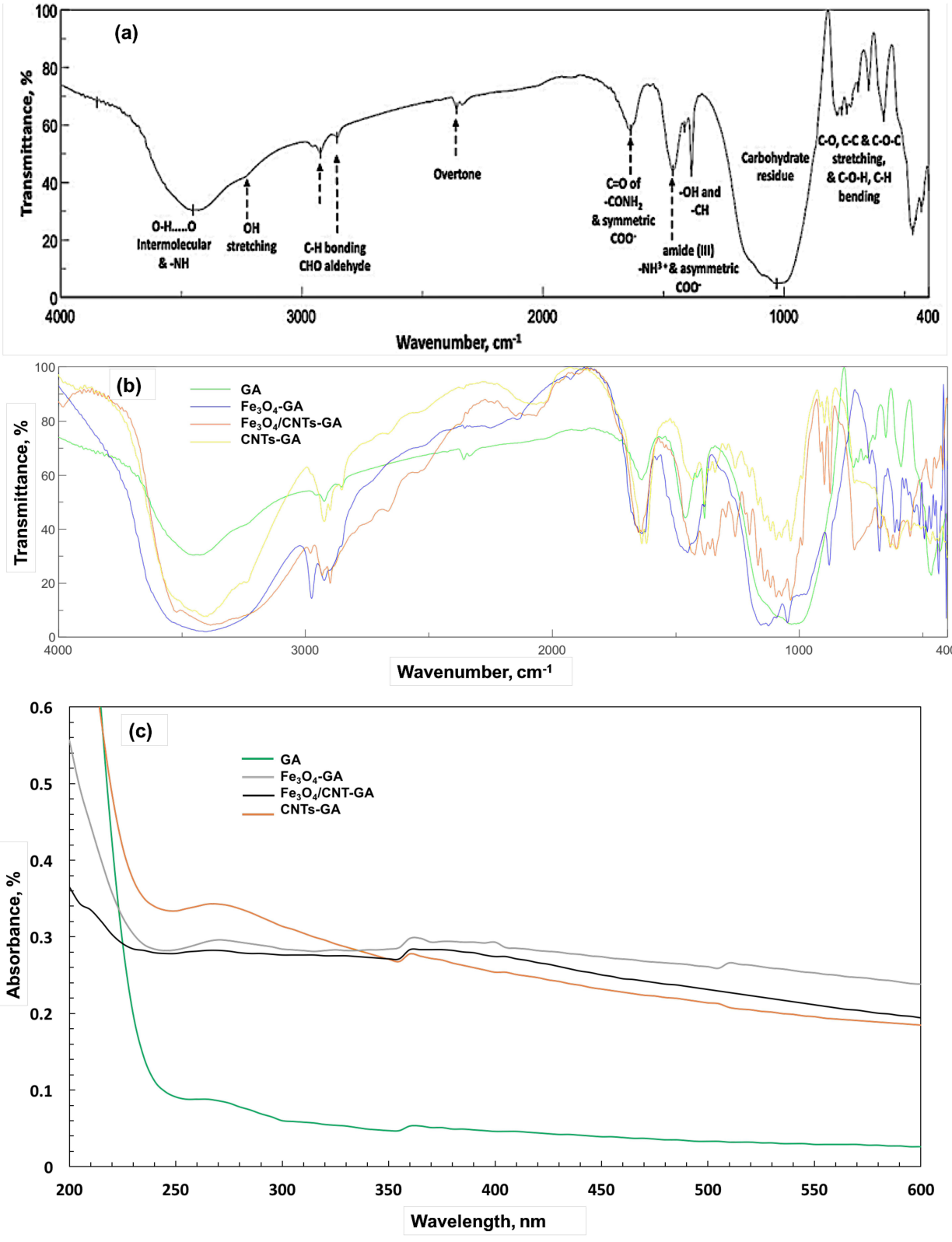

Figure 4 FTIR spectrum of the investigated GA (**a**) and the prepared nanoparticles stabilized by GA (**b**), and the UV-visible spectrum (**c**) of all the investigated nanoparticles.

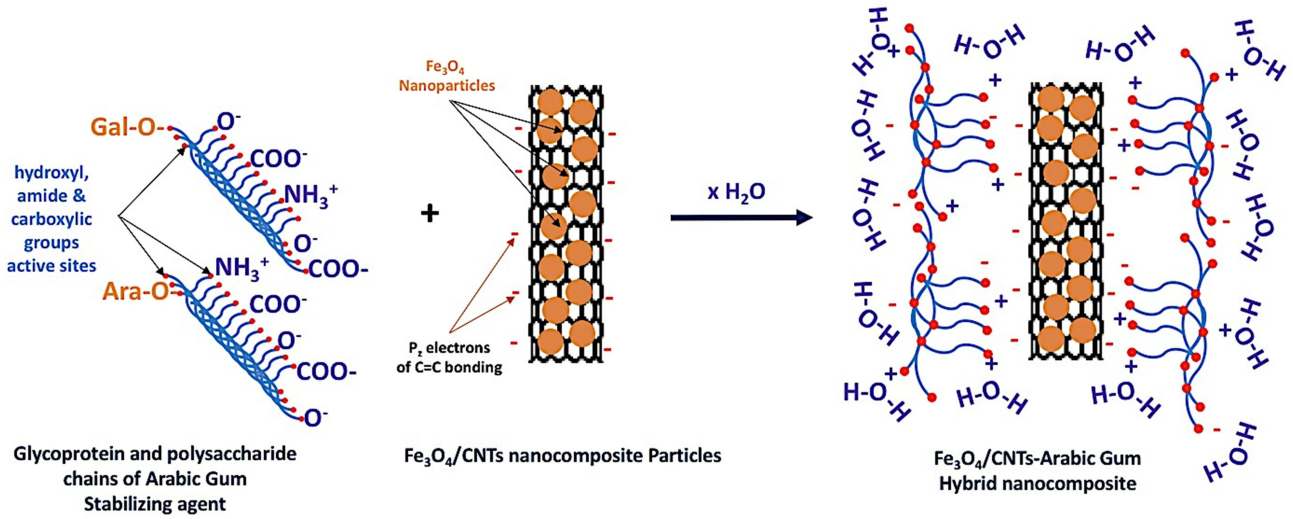

Figure 5 Schematic diagram of the interaction between the carbohydrate and the glycoprotein chains of the GA stabilizing agent and the synthesized Fe_3O_4 nanocomposite particles.

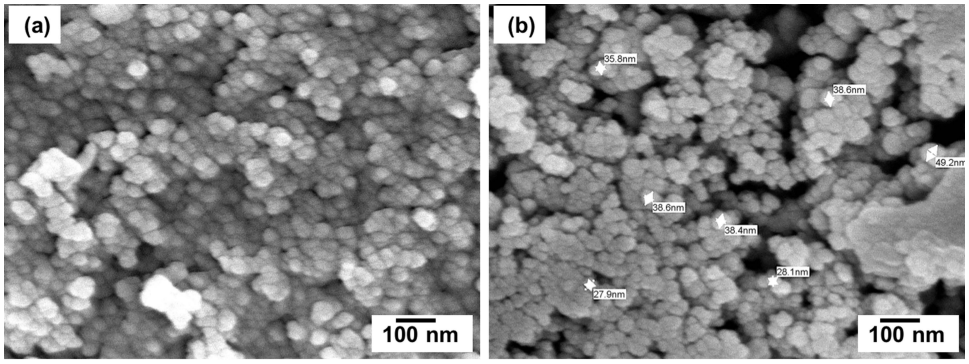

Figure 6 SEM of the prepared Fe_3O_4 NPs where (**a**) high magnification image and (**b**) high magnification image of particles size distribution.

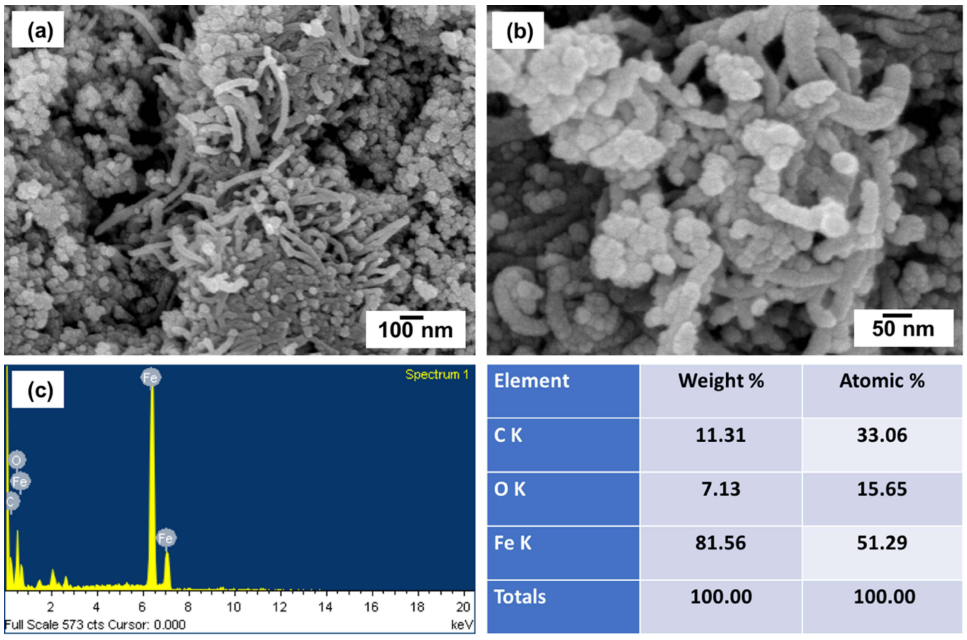

Element	Weight %	Atomic %
C K	11.31	33.06
O K	7.13	15.65
Fe K	81.56	51.29
Totals	100.00	100.00

Figure 7 SEM of GA-stabilized Fe_3O_4 NP with low and high magnifications (**a** and **b**), and EDS compositional analysis of GA-stabilized Fe_3O_4 NPs (**c**).

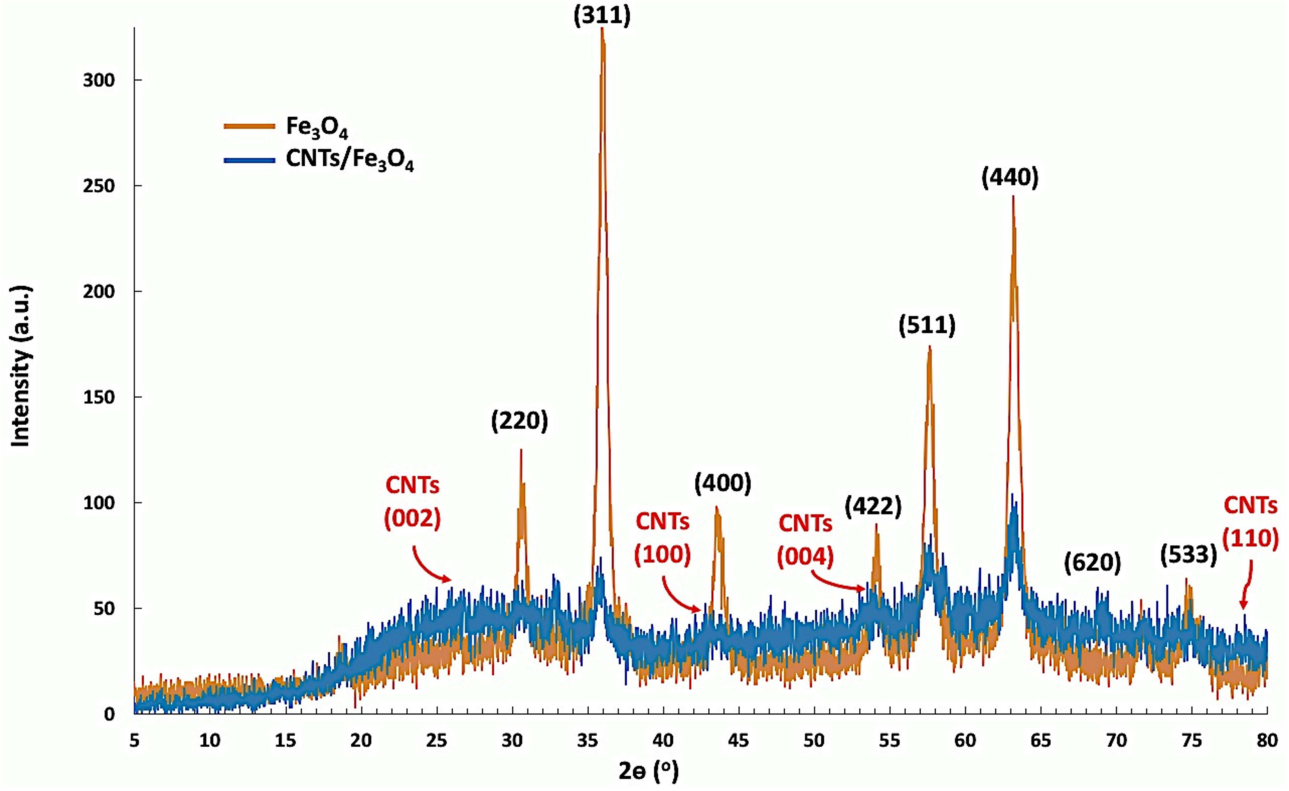

Figure 8 XRD patterns of the synthesized Fe_3O_4 and the Fe_3O_4/CNTs nanocomposite particles.

SLC40A1 Expression Analysis

The gene SLC40A1, which codes for the protein ferroportin that exports iron, was found to have significantly lower levels of expression in the myeloid leukemia cell lines studied (Kasumi-1, HL-60, and THP-1) compared to normal primary bone marrow $CD34^+$ cells. Among the cell lines, HL-60 had the lowest expression, followed by THP-1 and Kasumi-1 (Figure 10).

In vitro Cytotoxic Activity

A 72-hour treatment of normal hematopoietic cells (primary bone marrow $CD34^+$) or leukemia cell lines (Kasumi-1, HL-60, or THP-1) with varying concentrations of each nanoformulation revealed that GA alone did not have a significant impact on cell viability. This suggests that GA itself is nearly non-cytotoxic to both leukemia cell lines and normal hematopoietic cells. The combination of GA-stabilized/destabilized Fe_3O_4 NPs and CNTs, as well as their individual forms, exhibited notable cytotoxicity against the leukemia cell lines under investigation. The IC_{50} values for these formulations ranged from 42.437 to 189.842 μg/mL. Remarkably, GA-Fe_3O_4 NPs/CNTs exhibited the highest level of cytotoxicity, as evidenced by IC_{50} values of 42.437, 63.343, and 141.674 μg/mL in HL-60, THP-1, and Kasumi-1 cell lines, respectively. HL-60 cells had the highest sensitivity to growth inhibition caused by the investigated nanostructures, with an IC_{50} range of 42.437–96.901 μg/mL. THP-1 cells followed with an IC_{50} range of 57.681–138.465 μg/mL, and Kasumi-1 cells had an IC_{50} range of 90.725–189.842 μg/mL. Although the evaluated nanostructures showed significant growth inhibitory effect against the leukemia cell lines (IC_{50}: 42.437–189.842 μg/mL), they exhibited comparatively minimal cytotoxicity against normal hematopoietic cells (IC_{50}: 113.529–162.656 μg/mL). Compared to Fe_3O_4 NPs or CNTs used separately, the combination of Fe_3O_4 NPs and CNTs showed stronger growth inhibitory action. The IC_{50} values for this combination were 51.882 μg/mL in HL-60 and 57.681 μg/mL in THP-1. In contrast, Fe_3O_4 NPs alone exhibited more efficacy in reducing the growth of Kasumi-1 cells compared to either Fe_3O_4 NPs combined with CNTs or CNTs alone. It is worth mentioning that the combination of Fe_3O_4 NPs with CNTs in a nanocomposite significantly improved their ability to fight against leukemia cells, with the effectiveness varying depending on the kind of cell.

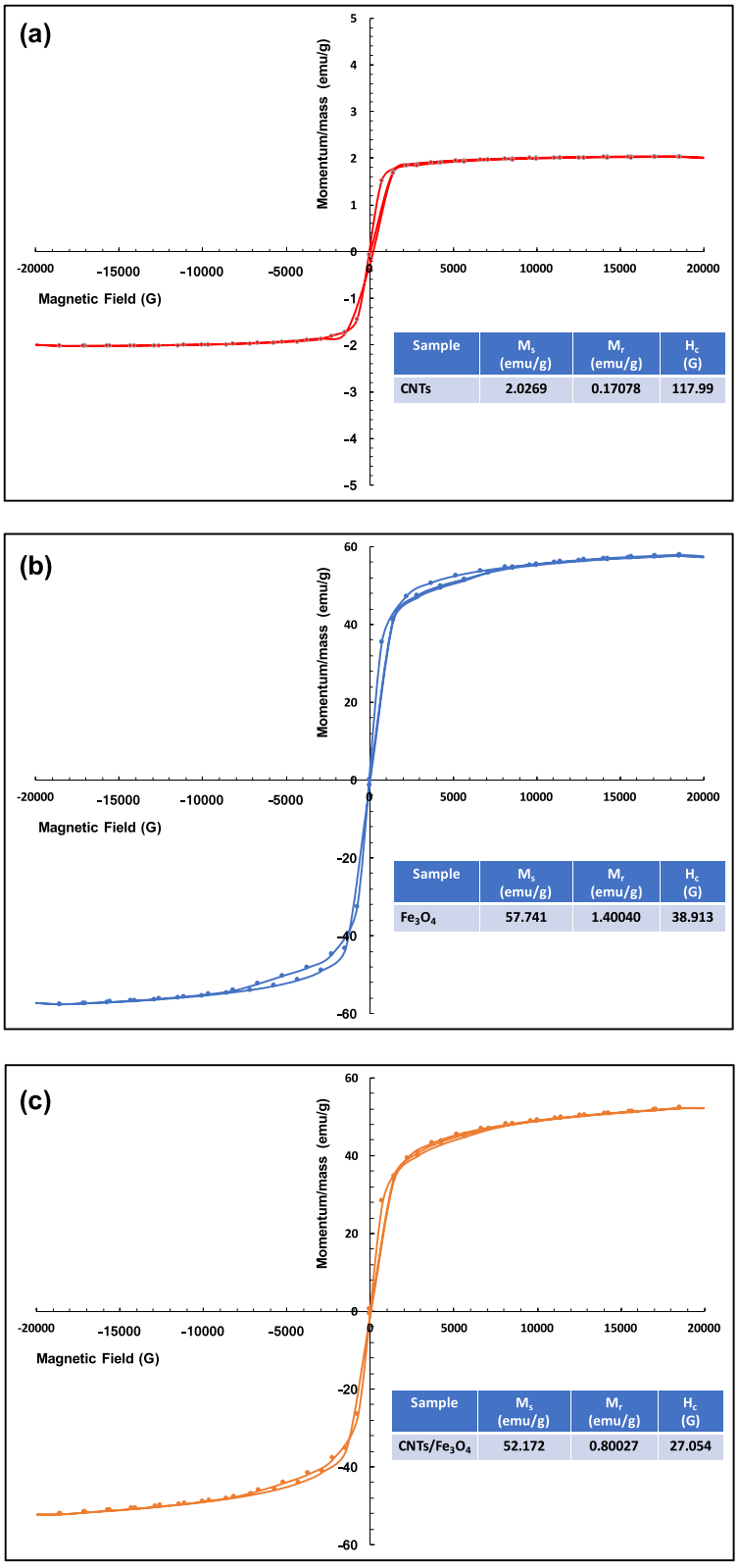

Figure 9 Magnetic hysteresis loops of the investigated CNTs (**a**), as well as the prepared Fe_3O_4 NPs (**b**) and the Fe_3O_4/CNTs nano-hybrid composite (**c**).

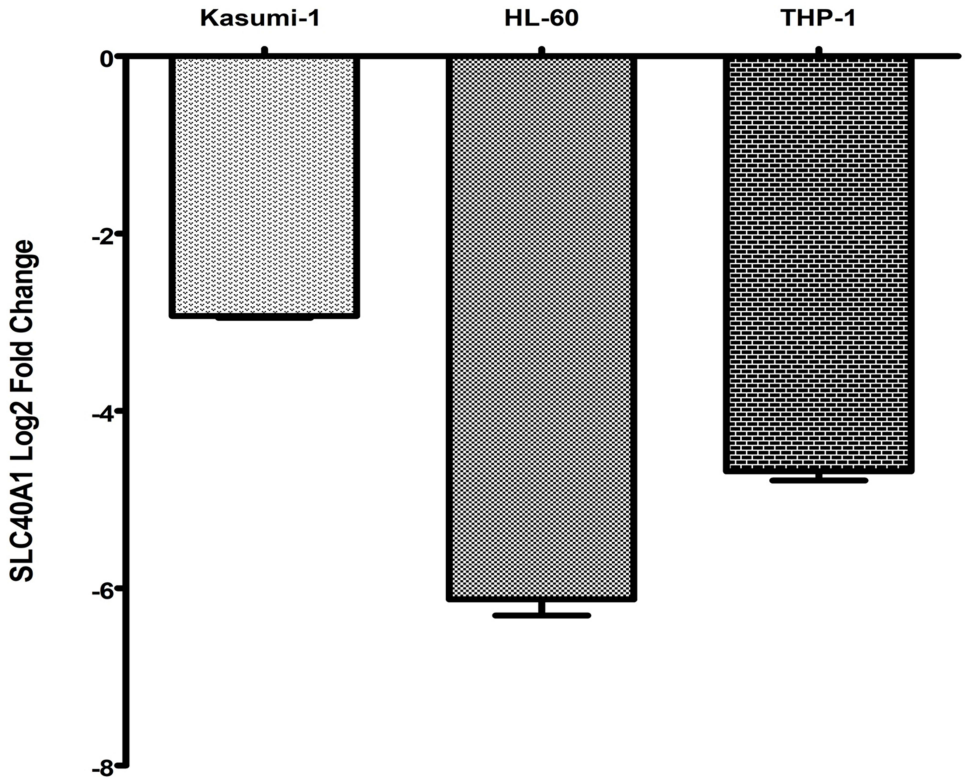

Figure 10 SLC40A1 gene expression levels in leukemia cell lines. Expression levels were measured in triplicate, and expressed as the fold change in gene expression in the treated cells normalized to the expression levels of the endogenous control and relative to normal primary bone marrow $CD34^+$ cells. Data are represented as mean ± SD of three independent experiments. SLC40A1 gene expression in Kasumi-1, HL-60 and THP-1 was significantly ($p < 0.05$) lower than that in primary bone marrow $CD34^+$ cells.

Furthermore, the use of GA to stabilize Fe_3O_4 NPs, CNTs, and Fe_3O_4 NPs/CNTs can enhance their ability to inhibit cellular proliferation, with the extent of this effect varying depending on the type of cell. Detailed anti-proliferative activity of the prepared nanostructures, against normal hematopoietic and leukemia cell lines is shown in Table 1.

Intracellular Iron Levels

A considerable increase in the amount of iron within the cells of the myeloid leukemia cell lines was seen after treating them with nanostructures containing Fe_3O_4 for 48 hours. Among the cell lines tested, Kasumi-1 exhibited the greatest levels of iron, followed by THP-1 and HL-60 (Figure 11A).

Intracellular ROS Concentrations

Quantifying intracellular ROS levels 48 hours after treatment with nanostructures revealed that HL-60 cells were the most influenced, with the highest elevation in ROS levels. This observation is consistent with the lowest expression of SLC40A1, as depicted in Figure 11B.

Mechanistic Investigations

Effect of the Prepared Nanoformulations on Apoptosis Induction

Fe_3O_4, CNTs, Fe_3O_4/CNTs, GA-Fe_3O_4, GA-CNTs, and GA-Fe_3O_4/CNTs all showed a large rise in early apoptotic HL-60 cells. The percentage of early apoptotic cells went from 0.04% in PBS-treated cells to 41.83%, 27.56%, 50.13%, 44.29%, 32.64%, and 54.58%, respectively. Additionally, doxorubicin (DXR) also resulted in a remarkable increase in early apoptotic cells, with a percentage of 47.92%. Similarly, the proportion of cells experiencing late apoptosis significantly increased from 0.13% in cells treated with PBS to 10.10%, 4.58%, 12.90%, 10.69%, 11.83%, and 11.85%, respectively. In contrast, DXR considerably boosted the percentage of late apoptotic cells to 9.50%. The results indicate that the produced nanostructures have a cytotoxic effect, partially through the activation of apoptosis (Figure 12A).

Table 1 In vitro Cytotoxic Activity of GA, Fe_3O_4, CNTs, Either Alone or in Combinations, Against Leukemia Cell Lines and Normal Hematopoietic Cells

	IC_{50} (μg/mL)			
	Leukemia Cell Lines			Normal Hematopoietic Cells
	Acute Myeloblastic Leukemia	Acute Promyelocytic Leukemia	Acute Monocytic Leukemia	Primary Bone Marrow $CD34^+$
	Kasumi-1	HL-60	THP-1	
DXR	0.142±0.006	0.045±0.003	0.465±0.034	0.857±0.127
GA	>1000	>1000	>1000	>1000
Fe_3O_4	122.954±27.368	67.915±8.246	115.703±14.632	162.656±23.476
CNTs	189.842±30.011	93.173±10.790	78.492±6.761	144.753±19.542
Fe_3O_4/CNTs	150.401±34.257	51.882±7.523	57.681±7.229	113.529±14.988
GA-Fe_3O_4	90.725±8.146	88.149±10.735	138.465±24.379	157.995±20.345
GA-CNTs	177.847±38.659	96.901±5.494	84.286±8.351	130.526±11.324
GA-Fe_3O_4/CNTs	141.674±26.325	42.437±3.776	63.343±11.860	114.324±17.235

Notes: IC_{50}, the concentration of the compound (μg/mL) producing 50% cell growth inhibition after 72 h of GA, Fe_3O_4, CNTs, either alone or in combinations, exposure. Results are represented as mean ± SD of three independent experiments.

Effect of the Prepared Nanoformulations on Cell Cycle Progression

Fe_3O_4, CNTs, Fe_3O_4/CNTs, GA-Fe_3O_4, GA-CNTs, and GA-Fe_3O_4/CNTs significantly increased the proportion of HL-60 cells in the G0/G1 phase from 53.4% in cells treated with PBS to 65.7%, 72.3%, 81.2%, 62.5%, 70.7%, and 79.0%, respectively. The

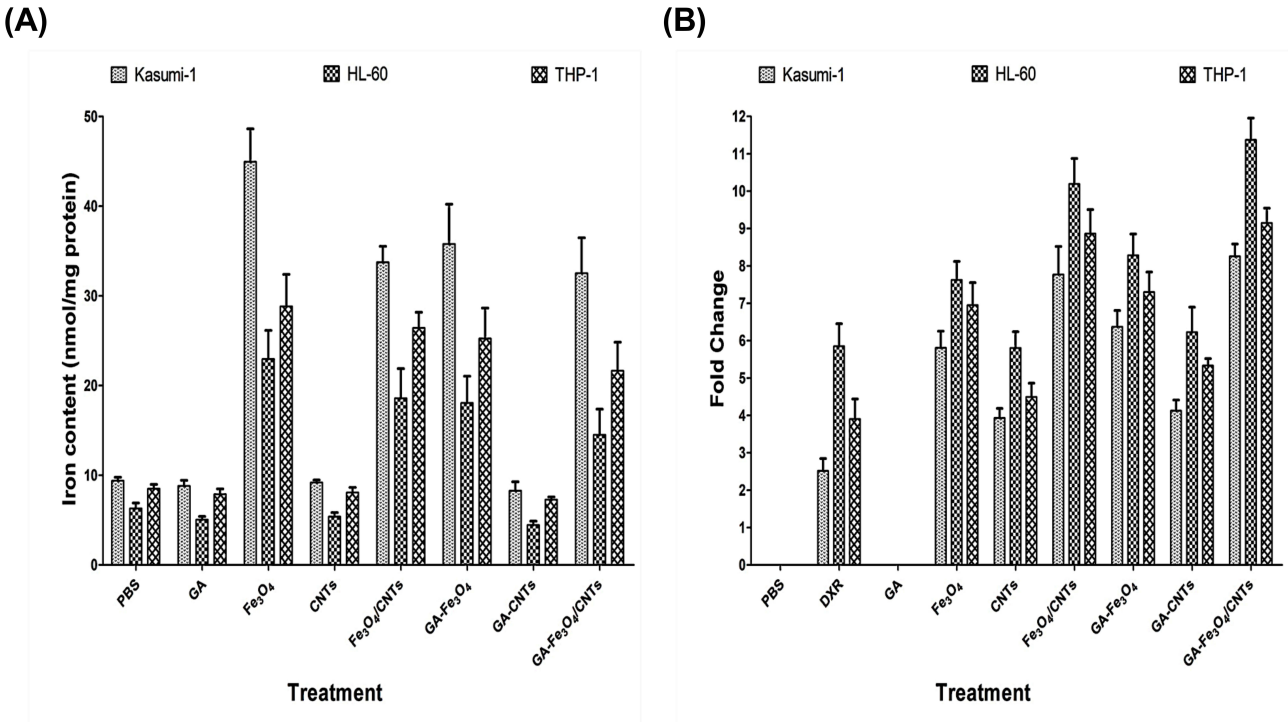

Figure 11 Effect of GA-stabilized/destabilized Fe_3O_4 NPs and CNTs, either alone or in combinations, on intracellular iron content (**A**) and ROS level (**B**) in leukemia cell lines. In all cell lines treated with Fe_3O_4-containing nanostructures, iron content was significantly ($p < 0.05$) higher than that in untreated cells. ROS level in all cell lines treated with GA-stabilized/destabilized Fe_3O_4 NPs and CNTs, either alone or in combinations, was significantly ($p < 0.05$) higher than that in untreated cells.

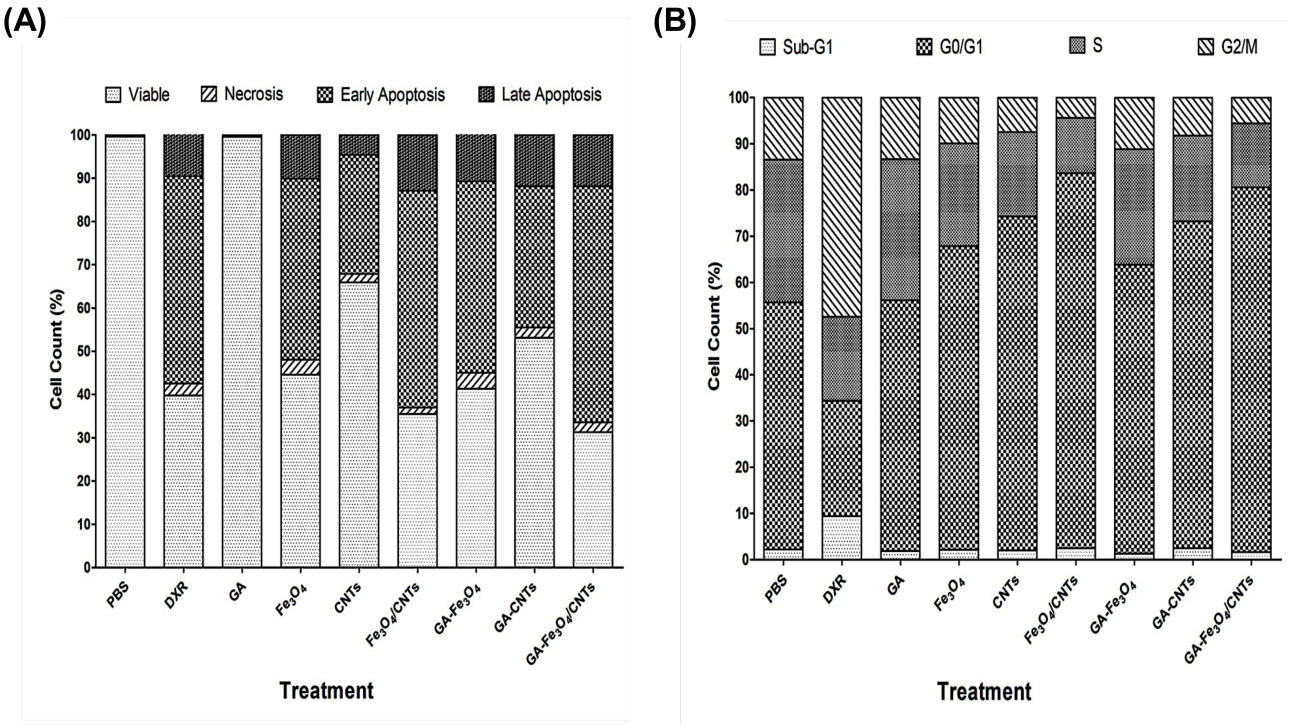

Figure 12 Effect of GA, Fe_3O_4, CNTs, either alone or in combinations, on apoptosis induction (**A**) and cell cycle progression (**B**) in in HL-60 cells. Data are represented as average percentage of three independent experiments.

population of cells in the S phase decreased significantly from 30.9% in PBS-treated cells to 22.2%, 18.2%, 11.9%, 25.0%, 18.5%, and 13.8%, respectively. Similarly, the population of cells in the G2/M phase decreased from 13.5% in PBS-treated cells to 10.0%, 7.5%, 4.5%, 11.2%, 8.3%, and 5.6%, respectively. The results suggest that the produced nanostructures may inhibit cell proliferation by causing cell cycle arrest at the G1 phase. Conversely, DXR significantly augmented the number of cells in the G2/M phase to 47.4%, while simultaneously reducing the population of cells in the S phase to 18.2% (Figure 12B).

Influence of the Prepared Nanoformulations on Apoptosis-Related Proteins

Treating HL-60 cells with different nanostructures, such as Fe_3O_4, CNTs, Fe_3O_4/CNTs, GA-Fe_3O_4, GA-CNTs, or GA-Fe_3O_4/CNTs, resulted in a significant increase in the level of the tumor suppressor protein p53. The increase was 4.67-fold, 0.86-fold, 2.54-fold, 3.80-fold, 0.22-fold, and 1.85-fold, respectively, compared to cells treated with PBS. Additionally, treatment with DXR caused a 4.53-fold increase in p53 concentration. The nanostructures that were examined resulted in a significant rise in the concentration of the pro-apoptotic protein BAX. The increases in BAX level were 0.63-fold, 3.44-fold, 2.02-fold, 1.24-fold, 5.16-fold, and 2.68-fold, respectively, compared to cells treated with PBS. In comparison, DXR caused a 3.01-fold increase in BAX levels. Similarly, the nanostructures that were tested resulted in a significant increase in the amount of the electron transport chain protein cytochrome C in the. The increase was 5.95-fold, 3.49-fold, 11.10-fold, 4.30-fold, 2.70-fold, and 7.02-fold, respectively, compared to cells treated with PBS. In contrast, DXR caused a 2.67-fold increase in the concentration of cytochrome C. In the same way, the nanostructures that were tested caused a significant increase in the concentration of caspase-3, an executioner protein of apoptosis, by 90082.33-, 56,415.67-, 135,465.67-, 110,799.00-, 72,115.67- and 163815.67-fold compared to cells treated with PBS. Additionally, DXR resulted in a 99715.67-fold increase in caspase-3 concentration. In contrast, the examined nanostructures did not have a notable suppressive impact on the levels of expression of the anti-apoptotic protein BCL-2 (Figure 13).

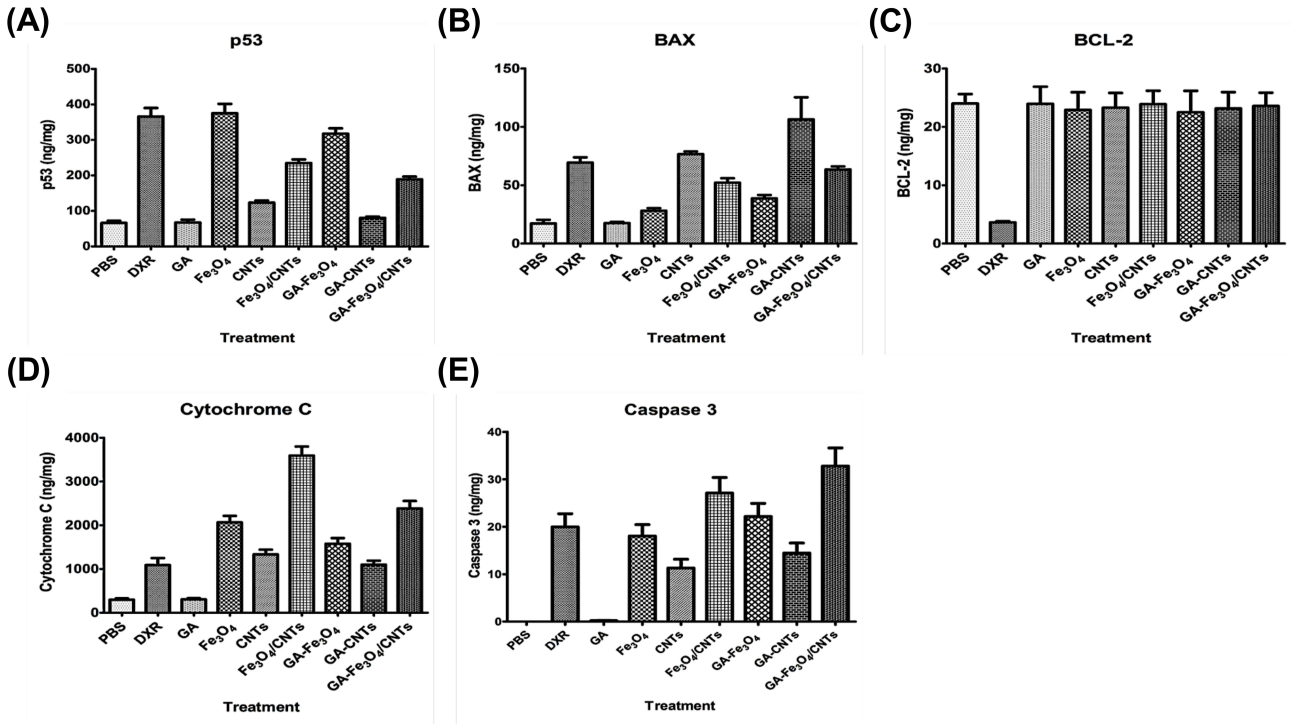

Figure 13 Influence of GA, Fe_3O_4, CNTs, either alone or in combinations, on apoptosis-related proteins, including p53 (**A**), BAX (**B**), BCL-2 (**C**), cytochrome C (**D**) and caspase 3 (**E**) in HL-60 cells. The concentrations of apoptosis-related proteins were measured in triplicate, corrected for sample dilution, normalized to the total protein content of the cell lysates, and expressed as ng/mg total protein of cell lysate. Data are represented as mean ± SD of three independent experiments. Compared to untreated cells, protein expression level increases in p53, BAX, cytochrome C and caspase 3 induced by treatment of the cells with GA-stabilized/destabilized Fe_3O_4 NPs and CNTs, either alone or in combinations, were statistically significant ($p < 0.05$).

Impact of the Prepared Nanoformulations on the Expression of the Genes Encoding Oxidative Stress-Related Proteins and Cyclin-Dependent Kinase Inhibitors

Exposing HL-60 cells to Fe_3O_4, CNTs, Fe_3O_4/CNTs, GA-Fe_3O_4, GA-CNTs, or GA-Fe_3O_4/CNTs, resulted in a notable increase in the expression of SIRT1, FOXO3, NFE2L2, MAP3K5, CDKN1A, and CDKN1B genes. This overexpression was more pronounced compared to the effect caused by DXR (Figure 14).

Discussion

The prepared Fe_3O_4/CNTs and Fe_3O_4/CNTs-GA nano-hybrid composite can be used as nanocontainers for different human medical treatments, including magnetic hyperthermia, and as drug delivery/carrier/release in the treatment of tumors. Further, Gum Arabic, a natural polymer known for its usage in controlled drug delivery systems, is also a surface-active molecule capable of improving magnetic nanoparticle stability in aqueous solutions by providing steric stabilization. Gum Arabic has the ability to stabilize nanoparticles using the solid-liquid interface effect. Gum Arabic can be used as a coating material to help prevent the agglomeration of the nanoparticles in biological media. Biological media have relatively high salt concentrations that, in part, may give rise to the flocculation of particles, particularly in the nanometer regime. Given that iron oxide nanoparticles agglomerate during synthesis, additional agglomeration is not desirable for biological applications, especially targeted drug delivery. A protective, charged coating that responds is an ideal solution for this situation to minimize the reduction of the electric double-layer thickness at high salt concentrations.

The dispersion of magnetorheological NPs in solutions poses a substantial limitation to the utilization of magnetorheological fluid in biological systems. The incorporation of hollow NPs known as CNTs along with a matrix consisting of superparamagnetic Fe_3O_4 has the capability to generate a unique magnetorheological fluid that exhibits exceptional dispersion efficiency. The acid treatment method of CNTs is responsible for the modification of the CNTs' surface and the introduction of functional groups, such as carboxylic groups. Additionally, it facilitates the deposition of magnetite

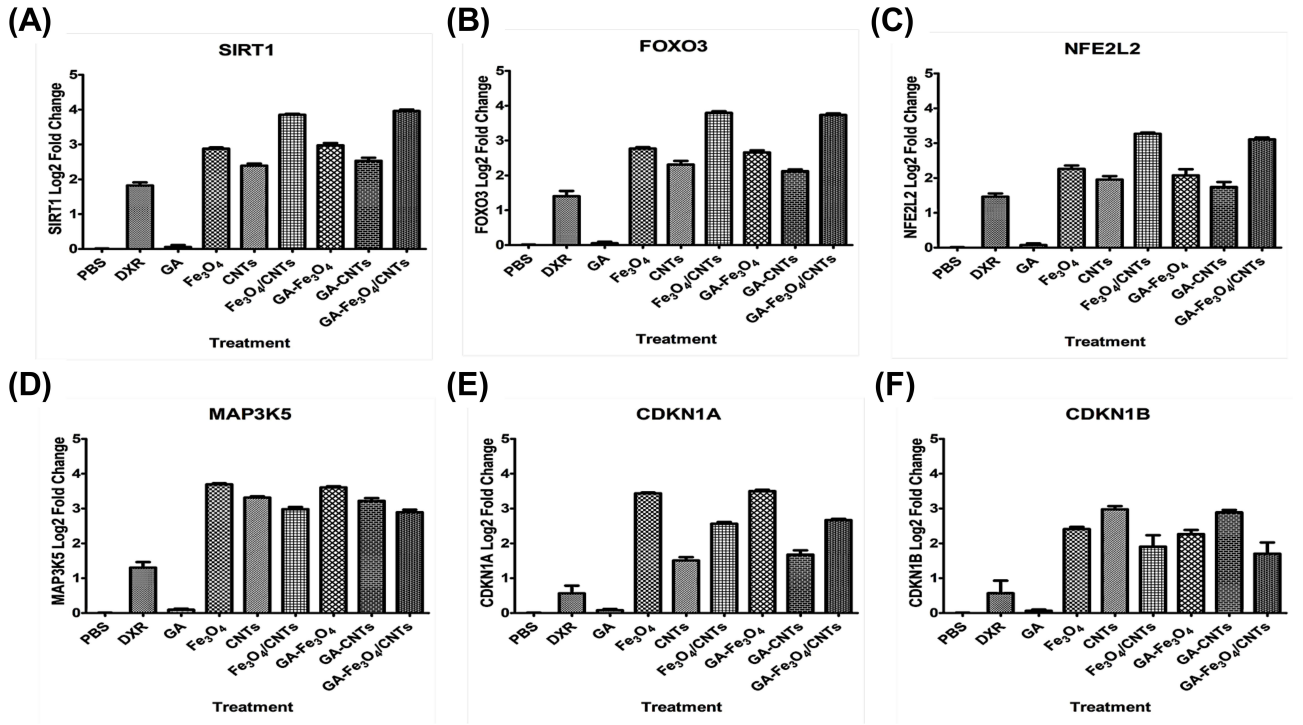

Figure 14 Impact of GA-stabilized/destabilized Fe_3O_4 NPs and CNTs, either alone or in combinations, on the expression of the SIRT1 (**A**), FOXO3 (**B**), NFE2L2 (**C**), MAP3K5 (**D**), CDKN1A (**E**) and CDKN1B (**F**) genes in HL-60 cells. Expression levels were measured in triplicate, and expressed as the fold change in gene expression in the treated cells normalized to the expression levels of the endogenous control and relative to the untreated cells. Data are represented as mean ± SD of three independent experiments. Compared to untreated cells, gene expression elevations in SIRT1, FOXO3, NFE2L2, MAP3K5, CDKN1A and CDKN1B induced by treatment of the cells with GA-stabilized/destabilized Fe_3O_4 NPs and CNTs, either alone or in combinations, were statistically significant ($p < 0.05$).

NPs on the graphitic surface of the CNTs [19,20]. The acid functionalization process of the CNTs resulted in the reduced crystallinity of some crystalline planes. Prior studies have indicated that the introduction of functional groups onto the graphitic surfaces of CNTs reduces their crystallinity.[21,22] Three hydroxos species, $Fe(OH)_3$ (aq), $Fe(OH)^{2+}$, $Fe(OH)^{-}_4$ are predominantly found in alkaline media. $Fe(OH)^{-}_4$ is the dominating species at pH values above 8, with a concentration of 97.8%. At a pH of 10.5, the $Fe(OH)^{-}_4$ and Fe^{2+} hydroxo condense to create the Fe_3O_4 phase.[23] The magnetite deposition reaction proceeded through the following reactions: $2Fe^{3+} + Fe^{2+} + 8OH- \rightarrow Fe_3O_4 + 4H_2O$ (1). The ultrasonic radiation had an impact on the deposition process, as suggested by our findings. Ultrasonic radiation promotes the generation of hydroxyl and hydrogen free radicals by breaking apart water molecules, which then triggers the creation of Fe_3O_4 NPs. Ultrasonic waves, capable of inducing cavitation, initiate a chemical reaction that leads to oxidation, reduction, dissolution, breakdown, and hydrolysis. Ultrasonic irradiation of aqueous liquids produces $H^{\bullet}$ and $OH^{\bullet}$ free radicals. These radicals have the ability to combine again to revert back to their original state or combine to form H_2 and H_2O_2.These powerful oxidizing and reducing agents are then used in different sonochemical reactions in aqueous solutions as shown in the following reactions: $H_2O \rightarrow H^{\bullet} + OH^{\bullet}$ (2); $H^{\bullet} + H^{\bullet} \rightarrow H_2$ (3); $OH^{\bullet} + OH^{\bullet} \rightarrow H_2O_2$ (4). The powerful oxidizing agent H_2O_2 triggers the oxidation of Fe^{2+} ions and the creation of the Fe_3O_4 NPS according to the following reactions: $2\ Fe^{2+} + H_2O_2 \rightarrow 2\ Fe^{3+} + 2OH^{-}$ (5); $Fe^{2+} + 2Fe^{3+} + 8\ OH^{-} \rightarrow Fe_3O_4 + 4H_2O$ (6).[24]

Previous reports have indicated that GA mostly consists of carbohydrates and protein macromolecules, which have the ability to rapidly encapsulate both Fe_3O_4 and Fe_3O_4/CNTs nanocomposite particles, hence preventing their aggregation in aqueous or polar conditions. The presence of surface active functional groups in GA enables it to attract and bind to the surface of Fe_3O_4 NPs and Fe_3O_4/CNTs nanocomposite particles. This prevents the particles from clumping together, enhances their stability, and facilitates their dispersion and stabilization in aqueous and polar solutions.[25] The FTIR spectra of the GA exhibited a wide band at 3451.96 cm^{-1}, indicating the existence of O-H….O intermolecular hydrogen bonding. This band is broad because to its overlap with the stretching band of -NH. The band observed at 3200 cm^{-1} was attributed to the O-H stretching mode. The primary bands seen at 2923.56 cm^{-1} and 2854.13 cm^{-1} were

attributed to the vibrational modes of the C-H group.[26] The band observed at 1635 cm^{-1} corresponds to the characteristic amide (I) band, which is attributed to the vibration of the C=O in the acetylated units (-$CONH_2$ groups) and the symmetric stretching of the COO- in carboxylic acid. Additionally, the strong band observed at 1535 cm^{-1} is associated with the amide (III) (-NH_3^+ groups) and the asymmetric stretching of the COO− in carboxylic acid.[27] The presence of the band observed at 1405 cm^{-1} can be attributed to the vibration of –OH, -CH, and –COOH groups in uronic acid.[28] The bands observed between 1250–800 cm^{-1} were attributed to the presence of the 1.4 linkage of galactose and 1.6 linkage of mannose, as well as the arabinogalactan carbohydrate residue of the GA.[29] Additionally, the stretching of C-O, C-C, and C-O-C bonds, as well as the bending modes of C-O-H and C-H in the GA polymer backbone, were also observed at lower wave numbers.[29,30] Also, FTIR spectrum of the Fe_3O_4-GA, Fe_3O_4/CNTs-GA exhibit the presence of magnetite phase by the typical strong band at 590 cm^{-1} which is related to the Fe-O bond as reported in the literatures.[31,32] This result evidences that our method allows the synthesis of the sole magnetite phase and also in the presence of the CNTs as well as GA.

The observed interaction between the carbohydrate and glycoprotein chains of the GA and the Fe_3O_4/CNTs nanocomposite particles can be attributed to the formation of a hybrid (Fe_3O_4/CNTs-GA) via the electrostatic attraction force between the negatively charged Fe_3O_4 NPs, that decorate the CNTs and the free electron in the Pz orbitals of the carbon atoms in the graphitic structure of the CNTs, and the various functional groups (amino, carboxylic, and hydroxyl groups) in the active site of GA, which aid in the dispersion and stabilization of the Fe_3O_4/CNTs nanocomposite particles in the aqueous solution.[33] On the other hand, the UV-visible spectrum of GA exhibit a wide peak of maximum absorbance at the wavelength of 270 nm due to the absorbance of tryptophan as reported in previous studies.[34,35] Tryptophan is very sensitive to the irradiation by UV radiation which is degraded under this condition and forming of hydroxyl radical ($^{\bullet}OH$).[36] However; due to the narrow band gap of the Fe_3O_4 nanoparticles; it exhibits a broad band in the UV and visible spectrum.[37]

The SEM micrographs of the generated Fe_3O_4/CNTs nanocomposite particles reveal an intense peak, indicating the presence of elemental carbon. This is attributed to the presence of CNTs and the carbon backbone of GA, as previously described.[38] Furthermore, the EDS compositional analysis reveals the absence of any further peaks, indicating the exceptional purity of the Fe_3O_4/CNTs nanocomposite particles that were synthesized. The CNTs under investigation underwent heat treatment to eliminate any organic substances that had contaminated the graphitic surfaces. Subsequently, the graphene surface was subjected to acid treatments using a mixture of H_2SO_4 and HNO_3 in order to functionalize it and add functional groups such as COOH, C=O, CH=O, and OH onto the surface. CNTs have a high specific surface area and numerous adsorption sites, although they can be classified as hydrophobic polymers mostly due to their carbon backbone. Therefore, the process of modifying the surface of CNTs and then applying a layer of Fe_3O_4 NPs might enhance the dispersion of CNTs in polar solutions, particularly in bodily fluids.[39] Qua et al fabricated a nanocomposite of CNTs and Fe_3O_4 using the co-precipitation method. In this process, Fe_3O_4 NPs with a size range of 10–30 nm were bonded to the surfaces of CNTs.[40] In a similar manner, Rahmawati et al utilized the sonochemical approach to fabricate nanocomposites of CNTs and Fe_3O_4, with the Fe_3O_4 NPs being evenly distributed over the CNT surfaces.[41] We hypothesized that this procedure has the potential to improve and augment the adhesion between CNTs and the magnetite NPs that are deposited on them.

The XRD analysis revealed the presence of low intensity peaks corresponding to the planes 002, 100, 004, and 110 of CNTs in the Fe_3O_4/CNTs nanocomposite. These peaks were discovered because of the little amount (1 wt. %) of CNTs present, which is below the detection limit of the XRD technique.[41] Previous investigations[42,43] have indicated that CNTs are classified as nonmagnetic materials, while possessing a magnetic moment that is not equal to zero. Several researchers have discovered that CNTs have diamagnetic properties. This is attributed to the presence of metallic impurities on their surfaces, which are introduced during the manufacturing process using catalytic techniques.[42–46] Nevertheless, CNTs can acquire ferromagnetic characteristics by merging with magnetic NPS, such as Fe_3O_4 NPs. When studying the magnetic properties of NPs, the magnetization (M) hysteresis curve can be obtained by subjecting the magnetic specimen to an external magnetic field of strength (H). This allows us to observe the relationship between M, which increases as H increases, until it reaches a maximum value called saturation magnetization (Ms). The magnetization curve exhibits a hysteresis loop due to the fact that not all domains revert back to their initial alignments when the

magnetic field (H) is lowered after reaching the saturation magnetization level. Therefore, once the magnetic field H reaches zero, there is a retentivity in the magnetization (Mr) that can only be eliminated by introducing a coercive field, known as coercivity (Hc), in the opposite direction to the original field. As the material's particle size drops to the nanoscale, the number of domains diminishes, eventually leading to the formation of a single domain at a critical particle size specific to the material. A magnetic material that exhibits an extremely narrow or nonexistent hysteresis loop is referred to as a superparamagnetic material.[41] Earlier reports have indicated that nanosized Fe_3O_4 demonstrates superparamagnetism and a lower saturation magnetization (Ms) value compared to bulk Fe_3O_4. Moreover, prior studies have shown that several factors can influence the saturation magnetization of the Fe_3O_4 NPs. The first factor relates to the entity of the spin disorder layer, which becomes more pronounced as the size of the Fe_3O_4 NPs decreases. The second factor can be attributed to the influence of a dipolar contact among the Fe_3O_4 NPs. The third factor is the uneven morphology of Fe_3O_4/CNTs NPs, which may affect the saturation magnetization value due to the contribution of surface anisotropy. Due to their nearly spherical shape, the produced Fe_3O_4 NPs are not predicted to have any contribution from surface anisotropy. Nevertheless, the Ms values noticeably dropped in the Fe_3O_4/CNTs nanocomposite particles. This might be attributed to the surface anisotropy of the manufactured Fe_3O_4/CNTs nanocomposite particles, which have a one-dimensional morphology. A further decrease in Ms could be ascribed to the incomplete crystallization of Fe_3O_4 following the co-deposition procedure. In addition, our findings indicated that all the samples exhibited extremely narrow hysteresis behaviors and displayed low values of coercivity (Hc) and retentivity (Mr). These findings demonstrate that the synthesized NPs display superparamagnetic characteristics at normal ambient temperature. This phenomenon occurs because magnetites NPs demonstrate superparamagnetic characteristics when their size is less than the critical size of the magnetic domain.[47]

The main reason for treatment failures in AML is the resistance of leukemic cells to chemotherapy-induced cell death and the development of multidrug resistance. Consequently, there is a significant demand for more efficient treatments for patients with AML.[48] Nanotechnology offers novel and auspicious alternatives to traditional approaches in combating cancer. The utilization of NPs that have been deliberately designed to treat cancer is an emerging area that has documented significant medical advancements.[49]

Many researches have extensively investigated the cytotoxic characteristics of Fe_3O_4 NPs and CNTs. However, the available data on their cytotoxicity profile is insufficient, ambiguous, and lacks a cohesive representation. Even while a number of studies have found that there is either no or very little cytotoxicity, others have found that there are significant cytotoxic effects. In addition, there is still a lack of a comprehensive knowledge of the potential lethal effects of Fe_3O_4 NPs and CNTs on AML cells, as well as the underlying biochemical pathways that are involved. In order to tackle these problems, we investigated the cytotoxic effects of GA-stabilized or destabilized Fe_3O_4 NPs and CNTs, both individually and in combination, on AML cell lines. We have demonstrated that the nanostructures we created are capable of triggering apoptosis in the cell lines we examined. The primary characteristic of iron oxide NPs is their specific ability to kill cancer cells, which is ensured by their specific absorption into cancer cells due to the high presence of anionic phospholipids on the cell membrane. The iron oxide NPs' specific activities, together with their limited toxicity to normal cells, have positioned them as highly promising nanoparticle formulations for cancer therapy based on nanotechnology.[50] Multiple studies have shown that iron oxide NPs greatly decreased the survival of various types of human cancer cells. An unregulated rise in iron accumulation results in heightened amounts of unbound iron, which engages in chemical processes involving free radicals such as Fenton and Haber-Weiss, leading to an excessive production of ROS and consequent oxidative stress. This process depletes antioxidants and ultimately triggers apoptosis. The cytotoxic effects of iron oxide NPs have been shown to differ depending on the kind of cells, indicating the intricate nature of the cytotoxic response to iron oxide NPs.[51]

CNTs have demonstrated the ability to cause cell death in several types of cells, resulting in the interruption of the cell cycle and programmed cell death. Cell damage caused by CNTs can be mediated through various Methods. CNTs have the ability to engage with receptors on the surface of cells, move across the cell membrane, and be absorbed by the cell. Upon entering the cell, CNTs have the ability to distribute themselves throughout the cytoplasm, become part of the subcellular structures, or mix with the nuclear membrane. They can even penetrate the nucleus and attach themselves to the DNA. These processes have been documented to initiate a wide range of inflammatory, oxidative stress, cell-killing,

and genomic changes. The growing body of evidence clearly indicates that the toxicity of CNTs to cells is caused by an excessive generation of ROS and the resulting oxidative stress.[52]

Remarkably, we have observed that the combination of Fe_3O_4 NPs with CNTs enhances the ability to kill cells in a manner that depends on the type of cell. This suggests that Fe_3O_4 NPs/CNTs nanohybrids can effectively merge the exceptional structural, optical, chemical, and thermal characteristics of both nanostructures into a distinct nanosystem that can be employed in cancer treatment approaches. The combination of metal NPs and carbon nanomaterials, which work together to produce enhanced effects, is a compelling and promising approach for creating nanohybrids with potential applications in biomedicine. These nanohybrids show promise for use in cancer therapy.[53]

We have observed that the anti-proliferative ability of Fe_3O_4 NPs and CNTs against the tested cell lines was improved by stabilizing them with GA. This improvement was dependent on the type of cell, indicating that the enhanced colloidal stability and biocompatibility of the Fe_3O_4 NPs and CNTs due to GA resulted in a significant increase in their anti-leukemic activity. The capacity of GA to function as a biocompatible enclosure for nanostructures has sparked significant enthusiasm in the field of nanotechnology. GA molecules possess charged functional groups (amino, carboxyl, and hydroxyl) that can adhere to the surface of various nanostructures through non-specific interactions. These groups serve as anchoring sites for the covalent bonding to NPs.[54] The surface charge of the stabilizer plays a crucial role in preserving the electrostatic contacts and steric hindrance between monodispersed NPs and the water system. Consequently, the poly-ionic characteristic of GA is vital in maintaining the uniformity of the NPs. GA improves the stability of NPs in water by preventing their agglomeration through the presence of its complex polysaccharide structures on the NPs surface. This effect is likely due to the steric repulsions mediated by the highly branched structures. Additionally, GA maintains the physicochemical properties of the NPs, increases their biocompatibility, and enhances their biological activity.[55]

Given the ability of the prepared nanostructures to induce apoptosis, we were motivated to investigate the specific molecular processes by which these nanostructures bring about their apoptotic effect. We assessed the amounts of apoptosis-related proteins in HL-60 cells that were treated compared to those that were not treated. The findings of our study demonstrated that the nanostructures we created mostly triggered apoptosis by upregulating the expression of p53, BAX, cytochrome C, and caspase-3 proteins. Apoptosis, a process of planned cell death, is directly linked to the activation of a group of proteases known as caspases, which are selective for aspartate and dependent on cysteine. Caspases can be categorized into initiator caspases (caspase-2, −8, −9, and −10) and effector caspases (caspase-3, −6, and −7) based on their position in cell death pathways. Apoptosis can be initiated by either the extrinsic or intrinsic routes. The two apoptotic routes come together to activate the effector caspases 3 and 7 by proteolysis, which is initiated by caspases 8 and 9. The effector caspases enzymatically cleave several cellular proteins, facilitating the generation of apoptotic bodies. Together, these caspase-induced activities spread the breakdown of the cell.[56] The p53 transcription factor, known as the "guardian of the genome" and the "cellular gatekeeper", functions by relaying various stress-inducing signals to trigger distinct cellular responses that inhibit cell proliferation. Therefore, the primary consequences of p53 activation are cell-cycle arrest and apoptosis. Upon activation of p53, specific cell types mostly experience apoptosis rather than cell-cycle arrest. P53 activates several genes that are involved in different stages of apoptosis signaling and execution. The capacity of p53 to trigger cell-cycle arrest and apoptosis possesses substantial antitumor efficacy that can be harnessed for the purpose of cancer therapy.[57]

We have shown that when HL-60 cells were exposed to nanostructures that were either stabilized or destabilized by GA, either alone or in combination, there was an increase in the proportion of cells in the G1 phase of the cell cycle. This prevented the cells from progressing from the G1 phase to the next phase. This effect was achieved by increasing the expression of genes that encode cyclin-dependent kinase inhibitors p21 and p27. Therefore, the growth-inhibiting impact of these nanostructures was, to some extent, caused by inducing arrest in the G1 phase. The cell cycle encompasses the series of events that a cell must undergo in order to undergo division. The cell cycle is comprised of distinct phases, namely G1, S, G2, and M, which consistently follow a specific sequence. The advancement of the cell cycle is primarily propelled and controlled by cyclin-dependent kinases (CDKs). The CDKs play a crucial role in facilitating the transition of cells from one phase of the cell cycle to the next, as well as in controlling whether cells are actively dividing or in a resting state. CDKs are controlled through their interaction with certain cyclins, which trigger and hinder phosphorylation processes. The functions of the CDKs differ during the cell cycle, as each one becomes active by physically binding

to its corresponding cyclin. The cyclins function as an endogenous indicator of a cell's cycling status and, if it is cycling, its specific stage within the cell cycle.[58]

The assembly and catalytic activity of cyclin/cyclin-dependent kinase (CDK) complexes are regulated by cyclin-dependent kinase inhibitors (CDKIs), a group of proteins that bind to cyclin/CDK complexes and reduce their activity. The intricate interplay among cyclin, CDK, and CDKI governs the progression of the cell cycle. CDKIs can be categorized into two categories according to their specific targeting of CDKs. The INK4 family members (p15, p16, p18, and p19) largely inhibit the activity of CDK4 and CDK6. On the other hand, the CIP/KIP family members (p21, p27, and p57) typically interact with cyclin D, E, A, and B-dependent kinase complexes by forming a binding complex.[59] p21, also referred to as cyclin-dependent kinase inhibitor 1A, is produced by the CDKN1A gene. It interacts with and hinders the operation of cyclin-CDK2, -CDK1, and -CDK4/6 complexes. As a result, it works as a suppressor of cell cycle advancement throughout the G1 and S phases of the cell cycle. The transcription of p21 is regulated by both p53-dependent and p53-independent pathways. P21 is a crucial downstream target of p53. Various types of cellular stressors, such as oxidative stress, increase the activity of p53 and subsequently enhance the expression of p21. Upon encountering excessive quantities of ROS, the p53 protein becomes activated, resulting in an upregulation of p21 expression. This can either cause a temporary pause in the G1 cell cycle or result in a long-term condition of senescence or apoptosis.[60] p27, sometimes referred to as cyclin-dependent kinase inhibitor 1B, is a crucial component involved in every stage of the cell cycle. It is encoded by the CDKN1B gene. p27 is unequivocally a key controller of G1 advancement. Furthermore, p27 serves as a crucial regulator of the G1→S transition. Additionally, it may have a role in regulating the progression of G2 phase and the completion of M phase and cytokinesis. p27 is a highly effective suppressor of several cyclin-CDK complexes. p27 has inhibitory effects on the catalytic activity of cyclin D-, E-, A-, and B-CDK complexes by interacting with both cyclin and CDK subunits. This interaction leads to the dissociation of cyclin from the CDK. Upon receiving signals that impede growth, the translation and stability of p27 are at their highest, leading to its buildup in the G0/G1 phase. Under favorable conditions for growth, the levels of p27 protein decrease fast due to a process called ubiquitin-dependent proteolysis. This allows for the activation of cyclin E-CDK2 and cyclin A-CDK2 complexes, which in turn facilitates the transition from the G1 phase to the S phase of the cell cycle.[61]

Our observations indicate that the introduction of GA-stabilized or destabilized nanostructures, either individually or in combination, to leukemia cell lines significantly enhances the production of ROS, which aligns with the observed decrease in cell viability. In HL-60 cells, consistent with the excessive production of ROS, we observed that the prepared nanostructures elevated the mRNA expression levels of genes that encode proteins related to oxidative stress, such as SIRT1, FOXO3, NFE2L2, and MAP3K5. Collectively, we hypothesized that the induced apoptosis by the prepared nanostructures is facilitated, to some extent, by the increased formation of ROS in leukemia cell lines. The capacity of Fe_3O_4 NPs and CNTs to produce ROS can be shifted from being a toxicological side effect to enhancing the effectiveness of chemotherapy. Previous research examined the impact of Fe_3O_4 NPs on two types of leukemia cells (KG1a and HL60). The results showed that only the viability of HL60 cells was considerably decreased when treated with Fe_3O_4 NPs. Conversely, the application of Fe_3O_4 NPs has not caused a substantial decrease in cell viability of KG1a, suggesting that KG1a cells exhibit greater resistance to Fe_3O_4 NPs. Furthermore, the administration of Fe_3O_4 NPs notably elevated the quantity of ROS in both types of cells.[62] In a previous study, the cytotoxic effects of ZnO/CNT@Fe_3O_4 nanocomposite on K562 cells generated from chronic myeloid leukemia were evaluated. The study showed that the nanocomposite dramatically reduced the viability of K562 cells. The production of cell cycle arrest and ROS-mediated apoptosis has been proposed as a potential explanation for the anticancer action of the ZnO/CNT@Fe_3O_4 nanocomposite.[63]

ROS are typically produced as an inherent result of cellular metabolism under normal physiological conditions. ROS, which is produced by mitochondria, plays a crucial role in regulating important cellular signaling pathways that are necessary for cell survival, growth, and differentiation. It is essential for maintaining cellular balance. However, excessive production of ROS leads to heightened oxidative stress, overpowering the cell's ability to protect itself with antioxidants. This results in harmful effects such as mitochondrial dysfunction and damage to biomolecules, ultimately leading to cell death.[64] ROS has a significant impact on hematopoiesis, specifically on the state and function of hematopoietic stem cells. Furthermore, it has been discovered that ROS has an impact on the characteristics of stemness and the rate of cell division in AML cells. Furthermore, numerous genetic abnormalities associated with the development

of AML impact the generation of ROS within cells, thereby facilitating oncogenic signaling mediated by ROS.[65] Mounting data indicates that cancer cells exhibit heightened sensitivity to levels of ROS in comparison to normal cells. This increased sensitivity renders cancer cells more vulnerable to cell death produced by oxidative stress, so presenting a promising treatment opportunity.[66]

Sirtuin 1 (SIRT1), which is produced by the SIRT1 gene, is a protein deacetylase that relies on nicotinamide adenine dinucleotide (NAD^+) for its activity. Mounting data suggests that SIRT1 functions as a regulatory mechanism in detecting and responding to oxidative stress. ROS induces the binding of c-Jun N-terminal protein kinase 1 (JNK1) with SIRT1, leading to the phosphorylation of SIRT1 by JNK1, hence enhancing SIRT1 activity. ROS has demonstrated the ability to regulate the activation of adenosine monophosphate-activated protein kinase (AMPK), a key controller of metabolic balance. AMPK activation stimulates NAD^+ production, hence triggering SIRT1 activation. SIRT1 activation effectively reduces ROS levels, therefore safeguarding against oxidative stress and enhancing cell viability. The function of SIRT1 seems to be facilitated by important transcription factors associated to redox signaling.[67] SIRT1 modulates two crucial transcription factors, p53 and FOXO, which have a significant impact on both cell survival and cell death. During periods of oxidative stress, the generation of ROS causes severe and irreversible damage to DNA. This damage triggers the stabilization and activation of p53, a protein that plays a crucial role in cell regulation. As a result, p53 promotes the production of pro-apoptotic proteins, which ultimately target the mitochondria and initiate the process of programmed cell death, known as apoptosis. SIRT1's deacetylation of p53 hinders p53's apoptotic action triggered by oxidative stress.[68] Like p53, the FOXOs trigger apoptosis in response to cellular stress. FOXOs not only promote apoptosis, but they also play a crucial role in cell survival. They achieve this by activating the transcription of genes that encode enzymes responsible for detoxifying ROS. In doing so, FOXOs help cells respond to oxidative stress. Thus, FOXOs play a dual function in both the promotion of cell death and the support of cell survival in response to ROS. The impact of SIRT1 on the functions of FOXOs is intricate and varies based on the specific target genes of FOXO. SIRT1 is recognized for its ability to remove acetyl groups from FOXO3, leading to the activation of FOXO3 and enhancing the production of genes that promote stress tolerance. At the same time, it suppresses the transcription of genes that are implicated in apoptosis. Therefore, SIRT1 seems to redirect the responses elicited by FOXOs from apoptosis towards stress tolerance, cell-cycle arrest, and ultimately favors cell survival.[69] FOXO3, which is produced by the FOXO3 gene, is widely acknowledged as a central controller of cellular stress response. FOXO3 is influenced by many cellular signals that primarily control its activity through posttranslational changes. These modifications direct FOXO3 to either the nuclear or mitochondrial compartment in response to stress stimuli. The FOXO3 protein is inactive in the cytoplasm and is transported either to the nucleus or to the mitochondria to carry out its transcriptional activities. FOXO3 mediates the transmission of signals from cellular stimuli to regulate the expression of target genes that are involved in the control of different cellular functions. When faced with oxidative stress, the activated FOXO3 increases the production of various ROS scavengers, such as superoxide dismutase 2 (SOD2) and catalase (CAT). This enhances the antioxidant response, which in turn reduces oxidative damage.[70] The transcription factor nuclear factor erythroid 2-related factor 2 (NRF2), derived from the NFE2L2 gene, is a key regulator of the cellular antioxidant defense system against oxidative damage. It activates the transcription of antioxidant genes downstream, thus contributing significantly to the maintenance of redox homeostasis. In the absence of stress, NRF2 interacts with Keap1, which is a component of the Cul3 ubiquitin E3 ligase complex. This interaction leads to the sequestration of NRF2 in the cytoplasm, followed by its ubiquitination and destruction by the proteasome. When there is oxidative stress, Keap1 gets oxidized. As a result, NRF2 separates from Keap1, moves to the nucleus, and attaches to specific DNA sequences called antioxidant response elements. These elements are found in the regulatory regions of the genes that NRF2 targets. This process leads to the transcriptional activation of cytoprotective genes, such as antioxidant enzymes and Phase II detoxifying enzymes.[71] The mitogen-activated protein kinase 5 (MAP3K5), also known as apoptosis signal-regulating kinase 1 (ASK1), is a member of the stress-responsive mitogen-activated protein kinase (MAP3K) family. It is encoded by the MAP3K5 gene. There has been a longstanding suggestion that the activity of MAP3K5 is initiated by various stresses, significantly contributing to apoptosis. Upon activation by a specific stressor, MAP3K5 initiates the phosphorylation of MKK4/7 and MKK3/6, which are mitogen-activated protein kinase kinases (MAP2Ks). Subsequently, these MAP2Ks activate c-Jun N-terminal kinase (JNK) and p38, respectively. JNK and p38 are stress-responsive mitogen-activated protein kinases (MAPKs) that are

crucial in mediating diverse stress responses. Excessive production of ROS is a highly effective stimulator of MAP3K5. The MAP3K5 is crucial in cellular reactions to oxidative stress, specifically, apoptosis generated by ROS, by continuously activating JNK and p38 signaling pathways, ultimately resulting in cell death.[72] As anticipated, the leukemia cells exhibited a noticeable rise in iron content following their exposure to nanostructures containing Fe_3O_4. Iron's capacity to acquire and release electrons allows it to engage in oxidation/reduction reactions, and consequently in reactions that generate free radicals. Oxidative stress occurs due to the abnormal buildup of iron and the resulting excess of ROS. This leads to damage to many biomolecules and can even induce cell death.[73] Mounting evidence suggests that the dysregulation of iron metabolism, which involves alterations in the import, storage, and export of iron within cells, plays a critical role in the genesis and progression of leukemia. Leukemia cells typically experience alterations in iron metabolism, leading to higher iron absorption and oxidative stress. This indicates that leukemia cells may be more susceptible to variations in iron and ROS levels compared to normal cells.[74] Multiple indications of heightened cellular iron levels have been discovered in patients with AML, suggesting a condition of excessive iron accumulation in this illness. Iron has been shown to worsen the symptoms of AML patients by contributing to bone marrow failure. Markers indicating excessive iron levels have been observed to be associated with a more unfavorable outcome in patients with AML.[75] Excessive accumulation of iron has been demonstrated to cause a halt in growth and the death of cells by triggering oxidative stress through the activation of p38 MAPK, JNK, and p53 pathways mediated by ROS in immature hematopoietic cells. Hence, strategies aimed at manipulating iron metabolism could offer novel perspectives for leukemia therapy.[76] The excessive buildup of ROS resulting from increased iron levels can trigger ferroptosis, a form of controlled cell death characterized by excessive lipid peroxidation. This mechanism can induce the death of leukemic cells. Research has demonstrated that leukemia cells frequently require a greater amount of iron compared to normal cells, as a result of their rapid division and strong oxidative metabolic activity. Leukemia cells are especially susceptible to ferroptosis due to their reliance on iron.[77] An effective anti-leukemia approach to trigger ferroptosis involves the utilization of iron-based nanomaterials.[78] Feraheme (ferumoxytol), a non-stoichiometric magnetite (superparamagnetic iron oxide) that has been approved by the FDA in 2009 for treating iron deficiency anemia in adult patients with chronic kidney disease,[79] exhibited an anti-leukemia effect in leukemic cells with low levels of ferroportin by triggering ferroptosis.[80]

The solute carrier family 40-member 1 (SLC40A1) gene encodes ferroportin, which is the sole known membrane iron exporter. Its main function is to assist in the release of iron from cells.[81] The dysregulation of ferroportin has been observed in AML. Decreased expression of the ferroportin gene in AML patients is strongly associated with increased sensitivity to chemotherapy, a favorable cytogenetics group, and improved overall survival. This suggests that ferroportin plays a significant role in the development, treatment response, and prognosis of AML patients. A greater susceptibility of this specific subtype of AML to the effects of chemotherapy may be a possible reason for the enhanced response to chemotherapy treatment observed in AMLs that have low levels of ferroportin expression. This model demonstrates that decreased levels of ferroportin result in increased levels of intracellular iron, subsequently leading to elevated levels of ROS production during exposure to ROS-inducing therapeutic drugs, such as chemotherapy. The increased intracellular levels of ROS, following chemotherapy, led to elevated levels of cell death and thus improved treatment outcomes.[82]

Our research has demonstrated that the expression of SLC40A1 is much lower in leukemia cell lines compared to normal primary bone marrow $CD34^+$ cells. This indicates a phenotype of abnormal iron export. Low levels of SLC40A1 make leukemia cells vulnerable to iron-induced production of ROS by taking advantage of the cells' inability to effectively remove excess iron in the form of Fe_3O_4 NPs. This excess iron leads to the generation of ROS that exceeds the cell's antioxidant capacity. The data indicate that leukemia cells with low SLC40A1 expression can be effectively targeted using oxidative ferrotherapy through the introduction of Fe_3O_4 NPs. Combinations of FDA-approved medications that generate ROS may provide the most immediate opportunities to eliminate leukemias with a poor iron export profile. The precise cause for the disparate cytotoxic impacts of Fe_3O_4 NPs and CNTs remains undisclosed. Multiple factors could account for the inconsistency observed in previous studies. Among these factors, the variations in size, shape, origin, quality, and dosage of the nanostructures used are particularly intriguing. These variations are likely to influence the mechanisms by which the nanostructures are taken up by cells and their interactions with different cellular components. On the other hand, the presence of different cell types being studied would impact the harmful effect caused

by the nanostructures. Another potential factor is that the method used to evaluate cytotoxicity could influence the cytotoxicity results of the tested nanomaterials. Therefore, it is necessary to conduct a more thorough and uniform assessment of the cytotoxic effects of Fe_3O_4 NPs and CNTs in order to reach a more definitive answer. To the best of our knowledge, our study is the first to reveal that GA has a strong ability to enhance the anti-leukemic effects of Fe_3O_4 /CNTs-GA nano-hybrid composite against AML cell lines. Furthermore, this study is the first to validate the synergistic impact of combining Fe_3O_4 NPs with CNTs in enhancing the anti-leukemic characteristics against AML cells.

Conclusions

Despite several investigations on the biological impacts of magnetite (Fe_3O_4) NPs and CNTs, there is still conflicting evidence regarding their cytotoxic effects. The existing knowledge is inconclusive, with a multitude of contrasting results. While some studies have shown little or no toxicity to cells, others have seen significant toxic effects. Moreover, there is currently a dearth of comprehensive knowledge on the potential lethal consequences and the molecular mechanisms involved in the impact of Fe_3O_4 NPs and CNTs on AML cells.

We report on the synthesis and characterization of Fe_3O_4 NPs as well as Fe_3O_4/CNTs-GA nano-hybrid composite stabilized in GA. Fe_3O_4 NPs, and Fe_3O_4/CNTs-GA nano-hybrid composite was fabricated using chemical deposition, employing ammonium hydroxide as the depositing agent at a temperature of 60°C under the effect of the ultrasonic radiation. The generated magnetite particles are at the nanoscale, whilst the Fe_3O_4/CNTs nano-hybrid composite have the coated type of Fe_3O_4 nano-layer deposited on their surface. The GA emulsifying agent was used as a powerful stabilizing agent of the prepared NPs in aqueous solution. The stabilized Fe_3O_4 NPs had a median particle size ranging from 23 to 28 nm, and exhibited a spherical shape. Both Fe_3O_4 NPs and the Fe_3O_4/CNTs-GA nano-hybrid composite have a superparamagnetic property with low coercivity values. The cytotoxic effects of GA-stabilized/destabilized Fe_3O_4 NPs and CNTs, either separately or together, were assessed against three myeloid leukemia cell lines. The study investigated the molecular mechanisms responsible for the cytotoxicity of the prepared nanostructures. This included estimating the iron content, measuring the level of ROS, estimating the number of apoptotic cells, analyzing the distribution of cell-cycle phases, determining the levels of apoptosis-related proteins, and quantifying the expression levels of genes encoding oxidative stress-related proteins and cyclin-dependent kinase inhibitors. The prepared nanostructures exhibited substantial cytotoxicity against the examined myeloid leukemia cell lines, while displaying comparatively minimal cytotoxicity towards normal hematopoietic cells. Presumably, the nanostructures that have been created exert their cytotoxic effect through various molecular mechanisms. They have the potential to enhance the generation of ROS, halt the progression of the cell cycle, and trigger programmed cell death. This was deduced from the ROS-induced elevation in the protein levels of p53, BAX, cytochrome C, and caspase-3, accompanied by the ROS-dependent enhancement of the genes encoding oxidative stress-related proteins and cyclin-dependent kinase inhibitors. Our data strongly support the potential use of Fe_3O_4 NPs/CNTs nanocomposite as a therapeutic intervention for AMLs, offering a novel perspective on leukemia treatment.

Data Sharing Statement

All data generated or analyzed during this study are included in this article.

Acknowledgments

The authors extend their appreciation to the Deanship of Scientific Research at Imam Mohammad Ibn Saud Islamic University (IMSIU) for funding and supporting this work through Research Partnership Program no RP-21-09-72.

Author Contributions

All authors made a significant contribution to the work reported, whether that is in the conception, study design, execution, acquisition of data, analysis and interpretation, or in all these areas; took part in drafting, revising or critically reviewing the article; gave final approval of the version to be published; have agreed on the journal to which the article has been submitted; and agree to be accountable for all aspects of the work.

Funding

This research was funded by the Deanship of Scientific Research at Imam Mohammad Ibn Saud Islamic University (IMSIU) through Research Partnership Program no RP-21-09-72.

Disclosure

The authors report no conflicts of interest in this work.

References

1. Döhner H, Wei AH, Appelbaum FR, et al. Diagnosis and management of AML in adults: 2022 recommendations from an international expert panel on behalf of the ELN. *Blood*. 2022;140:1345–1377. doi:10.1182/blood.2022016867
2. DiNardo CD, Erba HP, Freeman SD, Wei AH. Acute myeloid leukaemia. *Lancet*. 2023;401:2073–2086. doi:10.1016/s0140-6736(23)00108-3
3. Nirmala MJ, Kizhuveetil U, Johnson A, G B, Nagarajan R, Muthuvijayan V. Cancer nanomedicine: a review of nano-therapeutics and challenges ahead. *RSC Adv*. 2023;13:8606–8629. doi:10.1039/d2ra07863e
4. Das CGA, Kumar VG, Dhas TS, Karthick V, Kumar CMV. Nanomaterials in anticancer applications and their mechanism of action - A review. *Nanomed Nanotech Biol Med*. 2023;47:102613. doi:10.1016/j.nano.2022.102613
5. Długosz O, Matyjasik W, Hodacka G, et al. Inorganic Nanomaterials Used in Anti-Cancer Therapies: further Developments. *Nanomaterials*. 2023;13:1130. doi:10.3390/nano13061130
6. Keat C, Aziz A, Eid A, Elmarzugi N. Biosynthesis of nanoparticles and silver nanoparticles. *Bioresour Bioprocess*. 2015;2(47):1–11. doi:10.1186/s40643-015-0076-2
7. Prodan A, Iconaru S, Chifiriuc C, et al. Magnetic properties and biological activity evaluation of iron oxide nanoparticles. *J Nanomater*. 2013;2013(1):7. doi:10.1155/2013/893970
8. Das M, Goswami U, Ghosh SS, Chattopadhyay A. Bimetallic Fe–Cu nanocomposites on sand particles for the inactivation of clinical isolates and point-of-use water filtration. *ACS Appl Bio Mater*. 2018;1:2153–2166. doi:10.1021/acsabm.8b00572
9. Soenen J, Parak J, Rejman J, Manshian B. (Intra) cellular stability of inorganic nanoparticles: effects on cytotoxicity, particle functionality, and biomedical applications. *Chem Rev*. 2015;115:2109–2135. doi:10.1021/cr400714j
10. Eltarahony M, Abu-Serie M, Hamad H, et al. Unveiling the role of novel biogenic functionalized CuFe hybrid nanocomposites in boosting anticancer, antimicrobial and biosorption activities. *Sci Rep*. 2021;11:7790. doi:10.1038/s41598-021-87363-z
11. Zaki SA, Eltarahony MM, Abd-El-Haleem DA. Disinfection of water and wastewater by biosynthesized magnetite and zerovalent iron nanoparticles via NAP-NAR enzymes of *Proteus mirabilis* 10B. *Environ Sci Pollut Res*. 2019;26:23661–23678. doi:10.1007/s11356-019-05479-2
12. Baabu PRS, Kumar HK, Gumpu MB, Babu KJ, Kulandaisamy AJ, Rayappan JBB. Iron oxide nanoparticles: A review on the province of its compounds, properties and biological applications. *Materials*. 2022;16:59. doi:10.3390/ma16010059
13. Gao S, Xu B, Sun J, Zhang Z. Nanotechnological advances in cancer: therapy a comprehensive review of carbon nanotube applications. *Front Bioeng Biotechnol*. 2024;(12):1351787.
14. Sharma M, Alessandro P, Cheriyamundath S, Lopus M. Therapeutic and diagnostic applications of carbon nanotubes in cancer: recent advances and challenges. *J Drug Target*. 2024;32(3):287–299. doi:10.1080/1061186X.2024.2309575
15. Mauro N, Utzeri MA, Varvarà P, Cavallaro G. Functionalization of Metal and Carbon Nanoparticles with Potential in Cancer Theranostics. *Molecules*. 2021;26:3085. doi:10.3390/molecules26113085
16. Meng YQ, Shi YN, Zhu YP, et al. Recent trends in preparation and biomedical applications of iron oxide nanoparticles. *J Nanobiotechnol*. 2024;22(1):24. doi:10.1186/s12951-023-02235-0
17. Semenov KN, Ageev SV, Kukaliia ON, et al. Application of carbon nanostructures in biomedicine: realities, difficulties, prospects. *Nanotoxicology*. 2024;18(2):181–213. doi:10.1080/17435390.2024.2327053
18. Ashour MA, Fatima W, Imran M, Ghoneim MM, Alshehri S, Shakeel F. A Review on the Main Phytoconstituents, Traditional Uses, Inventions, and Patent Literature of Gum Arabic Emphasizing Acacia seyal. *Molecules*. 2022;27:1171. doi:10.3390/molecules27041171
19. Daoush WM, Lim BK, Mo CB, Nam DH, Hong SH. Electrical and mechanical properties of carbon nanotube reinforced copper nanocomposites fabricated by electroless deposition process. *Mater Sci Eng*. 2009;513–514,247–253. doi:10.1016/j.msea.2009.01.073
20. Daoush WM, Imae T. Fabrication of PtNi bimetallic nanoparticles supported on multi-walled carbon nanotubes. *J Exp Nanosci*. 2015;10:392–406. doi:10.1080/17458080.2013.838703
21. Daoush WM, Hong SH. Synthesis of multi-walled carbon nanotube/silver nanocomposite powders by chemical reduction in aqueous solution. *J Exp Nanosci*. 2013;8:742–751. doi:10.1080/17458080.2011.604959
22. Daoush WM, Lim BK, Nam DH, Hong SH. Microstructure and mechanical properties of CNT/Ag nanocomposites fabricated by spark plasma sintering. *J Exp Nanosci*. 2014;9:588–596. doi:10.1080/17458080.2012.680927
23. Compeán-Jasso ME, Ruiz F, Martínez JR, Herrera-Gómez A. Magnetic properties of magnetite nanoparticles synthesized by forced hydrolysis. *Mater Let*. 2008;62:4248–4250. doi:10.1016/j.matlet.2008.06.053
24. Riesz P, Berdahl D, Christman CL. Free radical generation by ultrasound in aqueous and nonaqueous solutions. *Environ Health Perspect*. 1985;64:233–252. doi:10.1289/ehp.8564233
25. Al-zharani M, Alyami NM, Qurtam AA, et al. Use of multi-walled carbon nanotubes (MWCNTs) stabilized in Arabic gum colloidal solution to induce genotoxicity and apoptosis of human breast and lung cancer cell lines. *Front Mater*. 2023;10.
26. Bashir M, Haripriya S. Assessment of physical and structural characteristics of almond gum. *Int J Biol Macromol*. 2016;93:476–482. doi:10.1016/j.ijbiomac.2016.09.009
27. Grant J, Cho J, Allen C. Self-assembly and physicochemical and rheological properties of a polysaccharide-surfactant system formed from the cationic biopolymer chitosan and nonionic sorbitan esters. *Langmuir*. 2006;22:4327–4335. doi:10.1021/la060017g

28. Qian F, Cui F, Ding J, Tang C, Yin C. Chitosan graft copolymer nanoparticles for oral protein drug delivery: preparation and characterization. *Biomacromolecules*. 2006;7:2722. doi:10.1021/bm060065f
29. Rezaei A, Nasirpour A, Tavanai H. Fractionation and some physicochemical properties of almond gum (Amygdalus communis L.) exudates. *Food Hydrocoll*. 2016;60:461–469. doi:10.1016/j.foodhyd.2016.04.027
30. Kizil R, Irudayaraj J, Seetharaman K. Characterization of irradiated starches by using FT-Raman and FTIR spectroscopy. *J Agri Food Chem*. 2002;50:3912–3918. doi:10.1021/jf011652p
31. E Bertolucci. Chemical and magnetic properties characterization of magnetic nanoparticles 2015 IEEE International Instrumentation and Measurement Technology Conference (I2MTC) Proceedings, *Pisa, Italy*, 2015, 1492–1496, *doi*: 10.1109/I2MTC.2015.7151498.
32. Lian-ying Zhang, Zhu X-J, Sun X-J, et al. Control synthesis of magnetic Fe_3O_4–chitosan nanoparticles under UV irradiation in aqueous system. *Curr Appl Phys*. 2010;10(3):828–833. doi:10.1016/j.cap.2009.10.002
33. Kumar PG, Kumaresan V, Velraj R. Stability, viscosity, thermal conductivity, and electrical conductivity enhancement of multi-walled carbon nanotube nanofluid using gum Arabic. *Fuller Nanotub Car Nanostruct*. 2017;25:230–240. doi:10.1080/1536383X.2017.1283615
34. Naeem S, Ahmed H, Mohammad S, Shafouri M. Investigation of Arabic gum optical properties as UV-Blue light down conversion for light emitting diode application. *J Phys Conf Ser*. 2020;1535.
35. Renard D, Lavenant-Gourgeon L, Ralet MC, Sanchez C. Acacia Senegal gum: continuum of molecular species differing by their protein to sugar ratio, molecular weight, and charges. *Biomacromol*. 2006;7:2637–2649. doi:10.1021/bm060145j
36. Zhang K, Fei W, Ji J, Yang Y. Degradation of tryptophan by UV irradiation: influencing parameters and mechanisms. *Water*. 2021;13:2368. doi:10.3390/w13172368
37. Cao Y, Li C, Li J, Li Q, Yang J. Magnetically separable Fe3O4/AgBr hybrid materials: highly efficient photocatalytic activity and good stability. *Nanoscale Res Lett*. 2015;10:251. doi:10.1186/s11671-015-0952-x
38. Kong H, Yang J, Zhang Y, Fang Y, Nishinari K, Phillips GO. Synthesis and antioxidant properties of gum Arabic-stabilized selenium nanoparticles. *Int J Biol Macromol*. 2014;65:155–162. doi:10.1016/j.ijbiomac.2014.01.011
39. Silva RCF, Ardisson JD, Cotta AAC, Araujo MH, Teixeira APC. Use of iron mining tailings from dams for carbon nanotubes synthesis in fluidized bed for 17α-ethinylestradiol removal. *Environ Pollut* 1987;260:114099. doi:10.1016/j.envpol.2020.114099
40. Qu S, Wang J, Kong J, Yang P, Chen G. Magnetic loading of carbon nanotube/nano-Fe(3)O(4) composite for electrochemical sensing. *Talanta*. 2007;71:1096–1102. doi:10.1016/j.talanta.2006.06.003
41. Rahmawati R, Melati A, Taufiq A, et al. Preparation of MWCNT-Fe3O4 Nanocomposites from Iron Sand Using Sonochemical Route. IOP Conference Series: Materials Science and Engineering 2017, 202, 012013, doi:10.1088/1757-899X/202/1/012013.
42. Tsui F, Jin L, Zhou O. Anisotropic magnetic susceptibility of multiwalled carbon nanotubes. *Appl Phys Lett*. 2000;76:1452–1454. doi:10.1063/1.126061
43. Kamil L, Manfred R, Albrecht L, Yulia K, Bernd B, Rüdiger K. Magnetic properties of carbon nanotubes with and without catalyst. *J Phys Conf Ser*. 2010;200:072061. doi:10.1088/1742-6596/200/7/072061
44. Torrens ON, Milkie DE, Ban HY, et al. Measurement of Chiral-Dependent Magnetic Anisotropy in Carbon Nanotubes. *J Am Chem Soc*. 2007;129:252–253. doi:10.1021/ja066719
45. Negri V, Cerpa A, López-Larrubia P, Nieto-Charques L, Cerdán S, Ballesteros P. Nanotubular paramagnetic probes as contrast agents for magnetic resonance imaging based on the diffusion tensor. *Angew Chem*. 2010;49:1813–1815. doi:10.1002/anie.200906415
46. Cerpa A, Köber M, Calle D, et al. Single-walled carbon nanotubes as anisotropic relaxation probes for magnetic resonance imaging. *Med Chem Comm*. 2013;4:669–672. doi:10.1039/C3MD20235F
47. Wang B, Wei Q-F, Qu S. Synthesis and Characterization of Uniform and Crystalline Magnetite Nanoparticles via Oxidation-precipitation and Modified co-precipitation Methods. *Int J Electrochem Sci*. 2013.
48. Shimony S, Stahl M, Stone RM. Acute myeloid leukemia: 2023 update on diagnosis, risk-stratification, and management. *Am J Hematol*. 2023;98:502–526. doi:10.1002/ajh.26822
49. Magro M, Venerando A, Macone A, Canettieri G, Agostinelli E, Vianello F. Nanotechnology-Based Strategies to Develop New Anticancer Therapies. *Biomolecules*. 2020;10. doi:10.3390/biom10050735
50. Alphandéry E. Bio-synthesized iron oxide nanoparticles for cancer treatment. *Int J Pharm*. 2020;586:119472. doi:10.1016/j.ijpharm.2020.119472
51. Paunovic J, Vucevic D, Radosavljevic T, Mandić-Rajčević S, Pantic I. Iron-based nanoparticles and their potential toxicity: focus on oxidative stress and apoptosis. *Chem Biol Int*. 2020;316:108935. doi:10.1016/j.cbi.2019.108935
52. Saleemi MA, Hosseini Fouladi M, Yong PVC, Chinna K, Palanisamy NK, Wong EH. Toxicity of Carbon Nanotubes: molecular Mechanisms, Signaling Cascades, and Remedies in Biomedical Applications. *Chem Res Toxi* 2021;34:24–46. doi:10.1021/acs.chemrestox.0c00172
53. Modugno G, Ménard-Moyon C, Prato M, Bianco A. Carbon nanomaterials combined with metal nanoparticles for theranostic applications. *Br J Pharmacol*. 2015;172:975–991. doi:10.1111/bph.12984
54. Ali BH, Ziada A, Blunden G. Biological effects of gum Arabic: a review of some recent research. *Food Chem Toxi*. 2009;47:1–8. doi:10.1016/j.fct.2008.07.001
55. Isobe N, Sagawa N, Ono Y, et al. Primary structure of gum Arabic and its dynamics at oil/water interface. *Carbohydr Polym* 2020;249:116843. doi:10.1016/j.carbpol.2020.116843
56. Bedoui S, Herold MJ, Strasser A. Emerging connectivity of programmed cell death pathways and its physiological implications. *Nat Rev Mol Cell Biol*. 2020;21:678–695. doi:10.1038/s41580-020-0270-8
57. Chen J. The Cell-Cycle Arrest and Apoptotic Functions of p53 in Tumor Initiation and Progression. *Cold Spring Harbor Perspectives in Medicine*. 2016;6:a026104. doi:10.1101/cshperspect.a026104
58. Panagopoulos A, Altmeyer M. The Hammer and the Dance of Cell Cycle Control. *Trends Biochem Sci*. 2021;46:301–314. doi:10.1016/j.tibs.2020.11.002
59. Jhaveri K, Burris Rd HA, Yap TA, et al. The evolution of cyclin dependent kinase inhibitors in the treatment of cancer. *Expert Rev Anticancer Ther*. 2021;21:1105–1124. doi:10.1080/14737140.2021.1944109
60. Georgakilas AG, Martin OA, Bonner, Bonner W M. W.M. p21: a Two-Faced Genome Guardian. *Trends Mol Med*. 2017;23:310–319. doi:10.1016/j.molmed.2017.02.001

61. Abbastabar M, Kheyrollah M, Azizian K, et al. Multiple functions of p27 in cell cycle, apoptosis, epigenetic modification and transcriptional regulation for the control of cell growth: a double-edged sword protein. *DNA Repair*. 2018;69:63–72. doi:10.1016/j.dnarep.2018.07.008
62. Luo T, Gao J, Lin N, Wang J. Effects of Two Kinds of Iron Nanoparticles as Reactive Oxygen Species Inducer and Scavenger on the Transcriptomic Profiles of Two Human Leukemia Cells with Different Stemness. *Nanomat*. 2020;10:1951. doi:10.3390/nano10101951
63. Yousefi AM, Safaroghli-Azar A, Fakhroueian Z, Bashash D. ZnO/CNT@Fe(3)O(4) induces ROS-mediated apoptosis in chronic myeloid leukemia (CML) cells: an emerging prospective for nanoparticles in leukemia treatment. *Artif Cells Nan Biotech* 2020;48:735–745. doi:10.1080/21691401.2020.1748885
64. Zhang B, Pan C, Feng C, et al. Role of mitochondrial reactive oxygen species in homeostasis regulation. *Redox Rep*. 27:45–52. doi:10.1080/13510002.2022.2046423
65. Sillar JR, Germon ZP, DeIuliis GN, Dun MD. The role of reactive oxygen species in acute myeloid Leukaemia. *Int J Mol Sci*. 2019;20:6003. doi:10.3390/ijms20236003
66. Shah MA, Rogoff HA. Implications of reactive oxygen species on cancer formation and its treatment. *Semin Oncol*. 2021;48:238–245. doi:10.1053/j.seminoncol.2021.05.002
67. Singh CK, Chhabra G, Ndiaye MA, Garcia-Peterson LM, Mack NJ, Ahmad N. The Role of Sirtuins in Antioxidant and Redox Signaling. *Antioxid Redox Sign*. 2018;28(8):643–661. doi:10.1089/ars.2017.7290
68. Achanta G, Huang P. Role of p53 in sensing oxidative DNA damage in response to reactive oxygen species-generating agents. *Cancer Res*. 2004;64:6233–6239. doi:10.1158/0008-5472.can-04-0494
69. Brunet A, Sweeney LB, Sturgill JF, et al. Stress-dependent regulation of FOXO transcription factors by the SIRT1 deacetylase. *Science*. 2004;303:2011–2015. doi:10.1126/science.1094637
70. Fasano C, Disciglio V, Bertora S, Lepore Signorile M, Simone C. FOXO3a from the Nucleus to the mitochondria: a round trip in cellular stress response. *Cells*. 2019;8:1110. doi:10.3390/cells8091110
71. He F, Ru X, Wen T. NRF2, a Transcription Factor for Stress Response and Beyond. *Int J Mol Sci*. 2020;21:4777. doi:10.3390/ijms21134777
72. Shiizaki S, Naguro I, Ichijo H. Activation mechanisms of ASK1 in response to various stresses and its significance in intracellular signaling. *Adv Bio Regul* 2013;53:135–144. doi:10.1016/j.jbior.2012.09.006
73. Dixon SJ, Stockwell BR. The role of iron and reactive oxygen species in cell death. *Nature Chemical Biology*. 2014;10:9–17. doi:10.1038/nchembio.1416
74. Brissot E, Bernard DG, Loréal O, Brissot P, Troadec MB. Too much iron: a masked foe for leukemias. *Blood Rev*. 2020;39:100617. doi:10.1016/j.blre.2019.100617
75. Weber S, Parmon A, Kurrle N, Schnütgen F, Serve H. The clinical significance of iron overload and iron metabolism in myelodysplastic syndrome and acute myeloid leukemia. *Front Immunol*. 2020;11:627662. doi:10.3389/fimmu.2020.627662
76. Wang F, Lv H, Zhao B, et al. Iron and leukemia: new insights for future treatments. *J Experimen Clin Can Rese*. 2019;38:406. doi:10.1186/s13046-019-1397-3
77. Lan H, Gao Y, Zhao Z, Mei Z, Wang F. Ferroptosis: Redox Imbalance and Hematological Tumorigenesis. *Front Oncol*. 2022;12:834681. doi:10.3389/fonc.2022.834681
78. Wang Y, Yang Y, Zheng X, et al. Application of iron oxide nanoparticles in the diagnosis and treatment of leukemia. *Front Pharmacol*. 2023;14:1177068. doi:10.3389/fphar.2023.1177068
79. Coyne DW. Ferumoxytol for treatment of iron deficiency anemia in patients with chronic kidney disease. *Exp Opin Pharmacother*. 2009;10:2563–2568. doi:10.1517/14656560903224998
80. Trujillo-Alonso V, Pratt EC, Zong H, et al. FDA-approved ferumoxytol displays anti-leukaemia efficacy against cells with low ferroportin levels. *Nature Nanotech*. 2019;14:616–622. doi:10.1038/s41565-019-0406-1
81. Rishi G, Subramaniam VN. Biology of the iron efflux transporter, ferroportin. *Adv Protein Chem Struct Biol*. 2021;123:1–16. doi:10.1016/bs.apcsb.2020.10.005
82. Gasparetto M, Pei S, Minhajuddin MS, Smith B, Seligman CA, Seligman P. Low ferroportin expression in AML is correlated with good risk cytogenetics, improved outcomes and increased sensitivity to chemotherapy. *Leukemia Res*. 2019;80:1–10. doi:10.1016/j.leukres.2019.02.011